Chapter 4
Advanced High-Strength Sheet Steels for Automotive Applications

Emmanuel De Moor

Abbreviations

AHSS	Advanced high-strength steels
AUST SS	Austenitic stainless steels
BH	Bake hardening
CCT	Continuous cooling transformation
CP	Complex phase
CS	Cold spot
DP	Dual phase
DQ	Drawing quality
EDS	Energy-dispersive spectroscopy
HER	Hole expansion ratio
HS	Hot spot
HSLA	High-strength low alloy
IA	Intercritical annealing
IF	Interstitial free
L-IP	Lightweight steels with induced plasticity
Low C	Low carbon
M	Martensite
PHS	Press-hardenable steels
PT	Partitioning temperature
Q&P	Quenching and partitioning
Q&T	Quench and tempered

E. DeMoor (✉)
Advanced Steel Processing and Products Research Center (ASPPRC), George S. Ansell Department of Metallurgical and Materials Engineering, Colorado School of Mines, Golden, CO, USA
e-mail: edemoor@mines.edu

R. Rana (ed.), *High-Performance Ferrous Alloys*,
https://doi.org/10.1007/978-3-030-53825-5_4

QT	Quenching temperature
RA	Reduction in area
SAZ	Shear-affected zone
SFE	Stacking fault energy
TBF	TRIP bainitic ferrite
TE	Total elongation
TEl	Total elongation
TRIP	Transformation-induced plasticity
TS	Tensile strength
TWIP	Twinning-induced plasticity
UEl	Uniform elongation
YPE	Yield point elongation
YS	Yield strength

Symbols

M_s	Martensite start temperature
M_f	Martensite finish temperature
$M_{\text{initial quench}}$	Initial martensite fraction based on Koistinen-Marburger equation
M_d	Temperature at which no transformation of austenite occurs
M_d^{30}	Temperature at which 50 pct of the originally present austenite volume fraction transforms to martensite at an applied strain of 30 pct
M_s^{σ}	Deformation temperature where the yield strength of the austenite equals the required stress for transformation to occur
$f_{\alpha'}$	Fraction of martensite
$\varepsilon_{\text{true}}$	True strain
C_i	Initial alloy carbon content
C_γ	Austenite carbon content
C_m	Martensite carbon content
T_A	Isothermal annealing temperature
γ_{final}	Austenite fraction following Q&P heat treating and assuming "idealized" partitioning

4.1 Introduction

Substantial research and implementation efforts are underway toward the development and application of advanced high-strength steels (AHSS) for automotive applications. These steels enable low-cost strategies to vehicle lightweighting by use of thinner sections that guarantee vehicle crash-worthiness and occupant protection while contributing to increased fuel efficiency. Consumer expectations

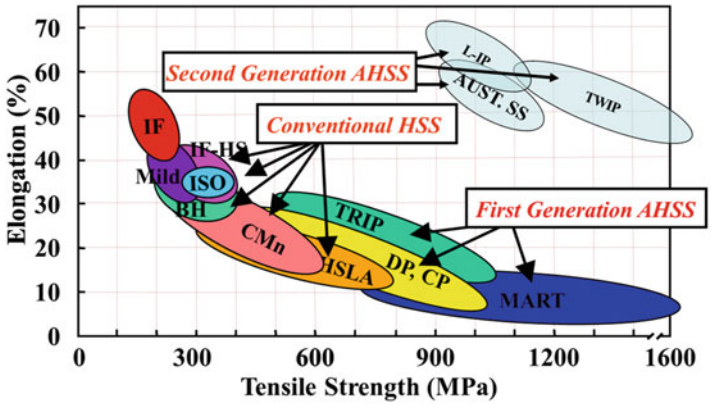

Fig. 4.1 Situation of tensile properties envelopes for conventional, first-generation AHSS transformation-induced plasticity (TRIP), dual-phase (DP), complex phase (CP), and martensitic (MART) steels, and second-generation twinning-induced plasticity (TWIP), lightweight steels with induced plasticity (L-IP), and austenitic stainless (AUST SS) steel grades on a total elongation versus tensile strength diagram [6, 7]

and regulatory pressure are driving increased emphasis on fuel efficiency and reduced tailpipe emissions [1–5].

The steel industry has responded to these needs and challenges by developing a variety of AHSS exhibiting varying strength and formability, alloy compositions, and microstructures. An overview of various AHSS grades is depicted in Fig. 4.1 on a total elongation versus tensile strength diagram [6, 7]. Dual-phase (DP), transformation-induced plasticity (TRIP), complex (CP), or multiphase steels are examples of AHSS commercially available at a variety of strength levels. The nomenclature has developed to further classify the grades into subcategories – first and second generation AHSS with DP, TRIP, CP and martensitic steels making up the first generation. These grades are characterized by lean alloying and heat-treating strategies to develop high-strength and high-ductility microstructures. First-generation AHSS have made substantial inroads into vehicle architectures as reflected in the pie charts shown in Fig. 4.2 for 2004 and 2017 steel usage breakdown for the same vehicle model, namely the Chevrolet Malibu [8, 9]. A reduction in the overall use of mild steel and replacement with AHSS is clearly observed. Lightweight metals also see an increase albeit at a more modest level in this selected example. Other vehicle architectures have chosen more intensive use of lightweight metals, in particular, aluminum for the body-in-white (BIW) [10–12].

The so-called second-generation AHSS employ high alloying levels to develop fully austenitic microstructures exhibiting high strength and exceptional ductility. Examples of these types of steels are twinning-induced plasticity (TWIP) and austenitic stainless [13]. Overall these grades have seen much less widespread implementation, predominantly due to increased cost and difficulties in processing. This chapter will review AHSS typically used for structural components in vehicle

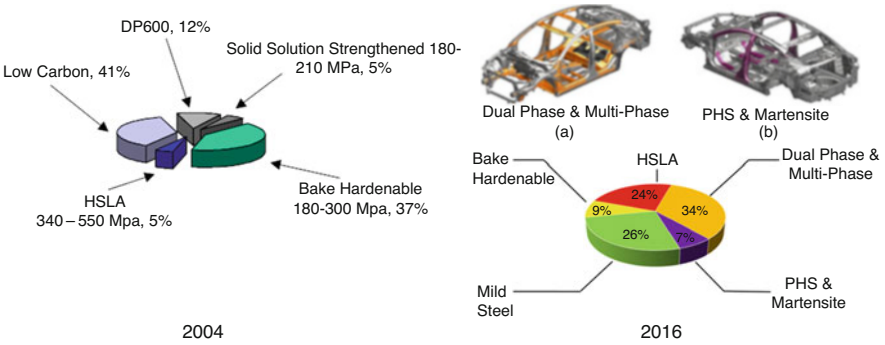

Fig. 4.2 Comparison of breakdown of steel grades used in a Chevrolet Malibu over time from 2004 to 2016 [8, 9]

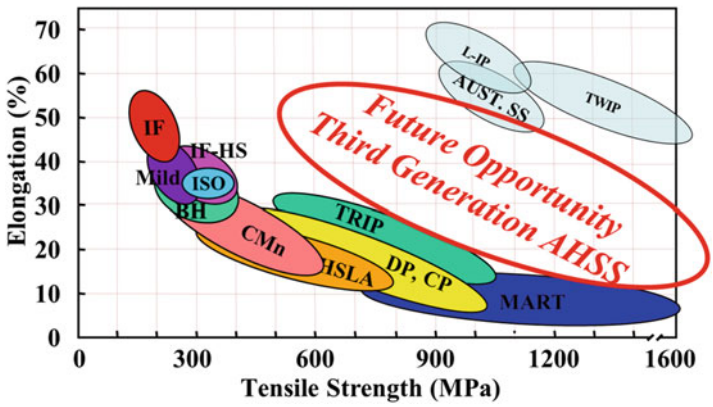

Fig. 4.3 Situation of the future opportunity third-generation AHSS tensile properties' envelope with respect to other steel grades on an elongation versus tensile strength diagram [6, 7]

architectures. A review of automotive steels for closures such as interstitial free (IF), bake hardening (BH), and drawing quality (DQ) grades can be found elsewhere [14].

More recently research and development efforts have been dedicated toward the development of so-called third-generation AHSS [6, 15]. This generation of steels is being developed to address the properties gap situated between the first-generation AHSS (i.e., DP, TRIP, CP, etc.) and martensitic steels, and the fully austenitic second-generation AHSS as shown in Fig. 4.3 by use of leaner chemistries than typically employed for the later-generation AHSS.

The above-discussed steel grades enable or are being developed for stamping operations where no additional thermal processing is required and the stamping takes place at room temperature. Another route which has seen widespread implementation is the so-called hot stamping or press hardening where the material is deformed at high temperature and accelerated cooled to set the final high-strength martensitic microstructure. This chapter will review various AHSS grades

in addition to hot stamping. Alloying, microstructures, and processing will be discussed.

4.2 Dual-Phase Steels

Dual-phase (DP) steels [16–18] have seen the most widespread use as AHSS in current vehicle architectures as illustrated in Fig. 4.2 [9]. The microstructure consists of ferrite and martensite as shown in Fig. 4.4 [19], and varying volume fractions of martensite are developed by using different reheating temperatures, which result in varying achievable strength levels and tensile properties. A range of strength levels can be achieved and are commercially available, e.g., DP590, DP780, DP980, and DP1180. The heat treatment involves reheating in the intercritical phase field and cooling to form martensite. Figure 4.5 shows processing thermal paths for cold-rolled (Fig. 4.6a) and hot-rolled (Fig. 4.6b) DP steels [20].

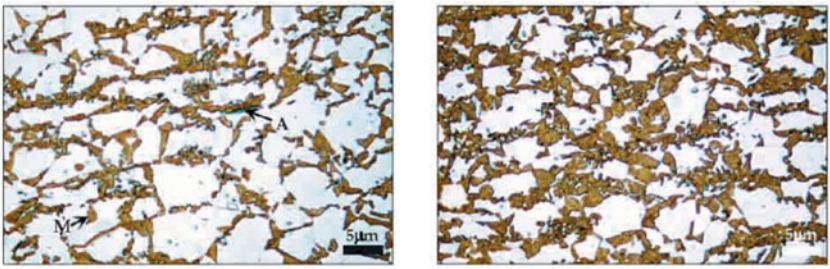

Fig. 4.4 Microstructures of DP steels quenched from (**a**) 775 °C and (**b**) 800 °C. Martensite (M) is straw color and ferrite is white, fine-retained austenite (A) also indicated [19]

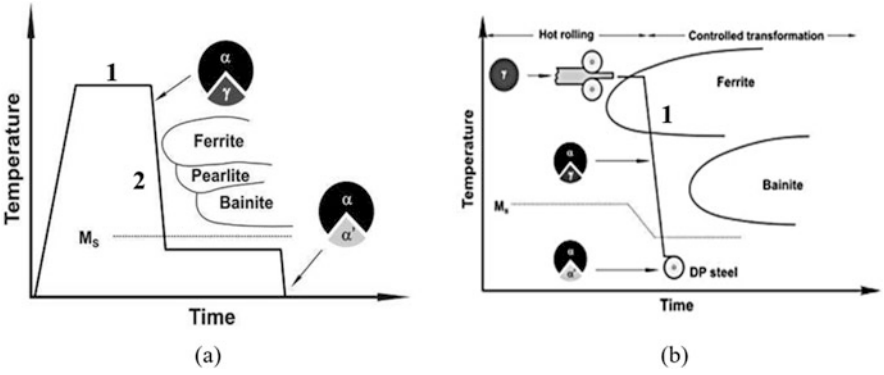

Fig. 4.5 Temperature-time plots for (**a**) cold-rolled and (**b**) hot-rolled DP steels [20]

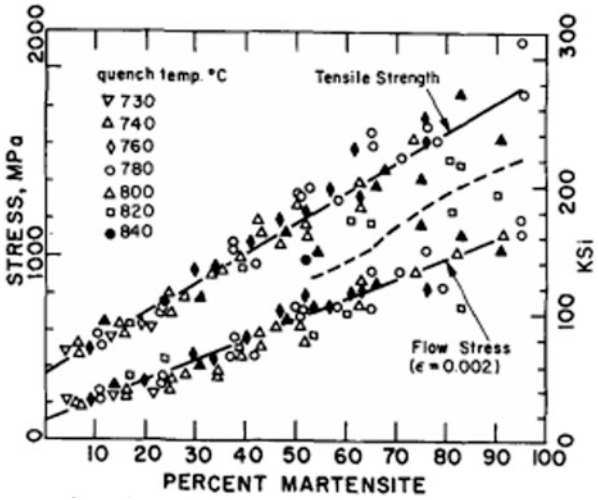

Fig. 4.6 Tensile strength and 0.2 pct offset flow stress as a function of percent (by volume) martensite for various Fe-C-Mn alloys and quenched from different intercritical annealing temperatures [22]

Judicious alloying is required to set hardenability for the desired microstructural requirement toward mechanical properties, and the levels of required alloying are processing dependent. Carbon, manganese, chromium, and molybdenum are prevalent additions [21]. Some fractions of bainite may be present depending on the effectiveness of the cooling step and the corresponding alloy design. Dual-phase steels are usually characterized by lean alloying, in particular, compared to TRIP steels and good weldability results, which has contributed to the widespread use of DP steels. Furthermore, the change in the ferrite fraction present at the intercritical annealing temperature allows for flexibility in setting strength levels. Data compiled by Davis [22] shown in Fig. 4.6 for a variety of Fe-C-Mn chemistries constituting in particular carbon alloying modifications show that strength levels increase with martensite level present or, conversely reduced intercritical ferrite levels. As shown in Fig. 4.6, the 0.2 pct offset flow stress and tensile strength for a variety of intercritical annealing temperatures and DP chemistries increase with increasing martensite fraction.

An example engineering stress-strain curve of a dual-phase steel is shown in Fig. 4.7 [23] and is compared to the engineering stress-strain curves of a plain carbon and high-strength low-alloy (HSLA) steel. Clearly greater tensile strength levels develop in a DP steel compared to the plain carbon predominantly ferritic steel and in this example similar to the included HSLA steel. The yielding behavior and strain hardening of the DP steel are however clearly different. Yielding at strength levels intermediate between the yield strength of the HSLA and plain carbon steel is followed by substantial strain hardening to equivalent ultimate tensile strength levels as the HSLA steel in this example. Round-house yielding behavior

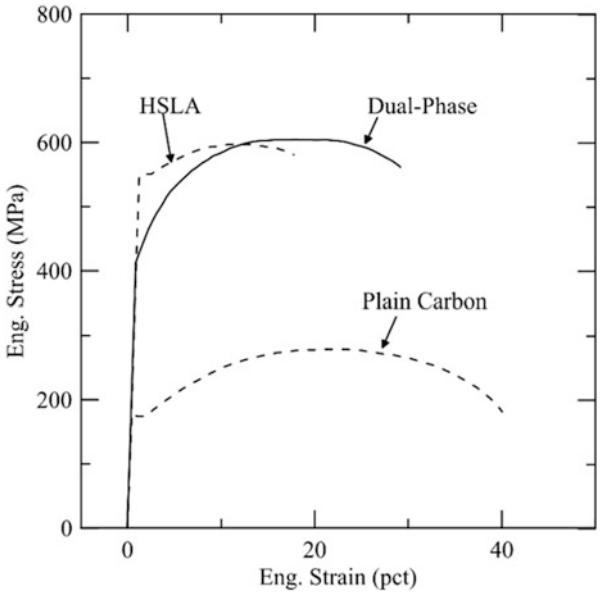

Fig. 4.7 Engineering stress-strain curves for plain carbon, HSLA, and DP steels. (Redrawn from [23])

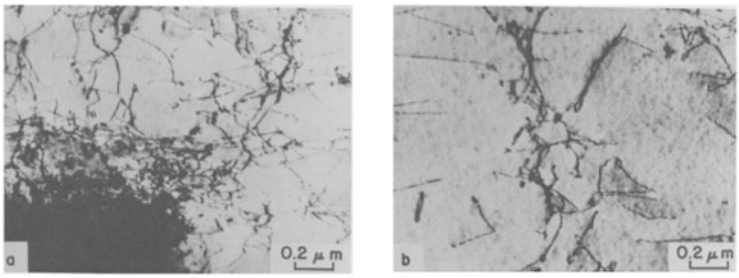

Fig. 4.8 TEM micrographs of DP microstructures showing dislocations (**a**) near a martensite-ferrite interface and (**b**) in a single ferrite grain away from the interface [24]

is observed characteristic of DP steels whereas the HSLA and plain carbon steels show yield point elongations. The round-house yielding results from the presence of mobile dislocations in DP microstructures introduced in the microstructure from the martensitic shear transformation and volume expansion–generating dislocations in the ferrite which remain unpinned during quenching and are mobile upon tensile testing. Figure 4.8 shows transmission electron micrographs of a DP steel where dislocations are abundantly present near the martensite-ferrite interface whereas a much lower density is observed away from the interface in the ferrite [24].

4.3 Transformation-Induced Plasticity Steels

Another family of first-generation AHSS is the transformation-induced plasticity or TRIP steels albeit these steels have seen less widespread applications in vehicle designs compared to DP steels. The TRIP effect refers to the transformation upon straining of meta-stable austenite [25], which positively impacts strain hardening and postpones necking to higher levels of strain. Metastable austenitic stainless steels such as AISI 304 exhibit the TRIP effect, and martensite progressively develops in the initial fully austenitic microstructure with increased strain resulting in increased strain hardening and superior formability [25]. Low-carbon TRIP steels for automotive BIW applications were developed to employ the TRIP effect in leaner and more cost-effective alloy chemistry. For instance, nickel is usually not added and manganese is added in limited quantities for hardenability rather than for austenite retention purposes. An austenite fraction of 10–20 vol pct is retained at room temperature by enrichment with carbon, which takes place during bainitic transformation. A heat-treating schematic to produce a low-carbon TRIP steel is provided in Fig. 4.9 [26].

Following reheating in the intercritical temperature range, the steel is accelerated cooled and held at a temperature in the bainitic transformation regime to develop a microstructure containing intercritical ferrite, bainitic ferrite, and retained austenite. As carbon is supersaturated in the bainitic ferrite, it needs to be rejected from the ferrite to alleviate the supersaturation. In the absence of alloying with Si and/or Al, this is done by the precipitation of cementite in the bainitic laths or in between the laths. The supersaturation can also be alleviated by stimulating the enrichment of the austenite remaining in the microstructure that requires alloying with Si and/or Al to suppress the formation of cementite due to its insolubility in cementite which reduces its growth kinetics [27]. Cementite suppression results in the remaining carbon available to enrich in austenite and as carbon is rejected from the growing

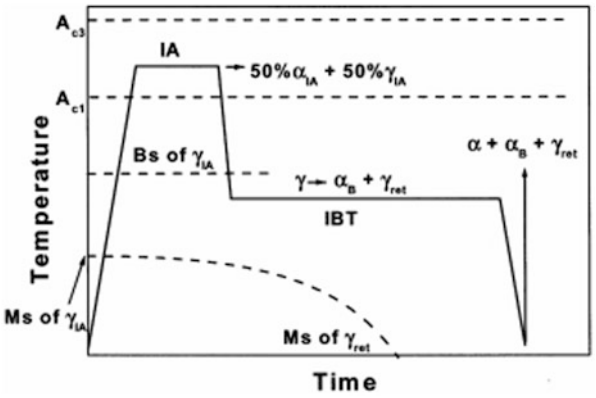

Fig. 4.9 Schematic of the thermal cycle for low-carbon TRIP steel processing, from [26]

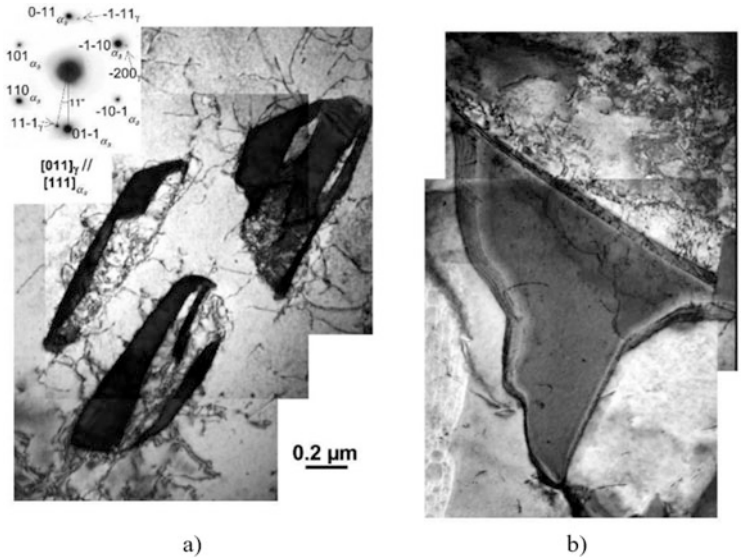

Fig. 4.10 Low-carbon TRIP steel microstructures showing (**a**) laths of bainitic ferrite and retained austenite and (**b**) a blocky retained austenite grain. Reproduced from [28]

bainitic laths, it enriches the remaining austenite and stabilizes it by lowering its martensite start temperature (M_s) as illustrated schematically in Fig. 4.9.

Representative TRIP steel microstructures are shown in Fig. 4.10 [28] where bainitic laths can be observed containing dislocations and where the darker laths were identified as austenite in Fig. 4.10a. A triangular grain of austenite is also included in Fig. 4.10b. The austenite is metastable, i.e., the austenite is retained at room temperature due to carbon enrichment but will transform to martensite when strain (or stress) is applied and is referred to as strain-induced (or stress-assisted) transformation. The degree of strain-induced transformation is strain dependent, and the evolution of the martensite fraction is shown in Fig. 4.11 as a function of true strain for three TRIP steel chemistries containing Si, Al, and a combination thereof [28]. The strain-induced martensite evolution with respect to strain exhibits a sigmoidal behavior that has been plotted using the Olson-Cohen model which assumes martensite embryos to form following the generation of nucleation sites such as shear-band intersections in the form of mechanical twins, dense stacking-fault bundles, and ε martensite [29]. A martensitic embryo is then able to nucleate on these intersections as more mechanical work is imparted. The sigmoidal behavior has been fitted with the Olson-Cohen model as expressed by according to [29]:

$$f_{\alpha'} = 1 - \exp\left[-\beta\left[1 - \exp\left(-\alpha\varepsilon\right)\right]^n\right] \tag{4.1}$$

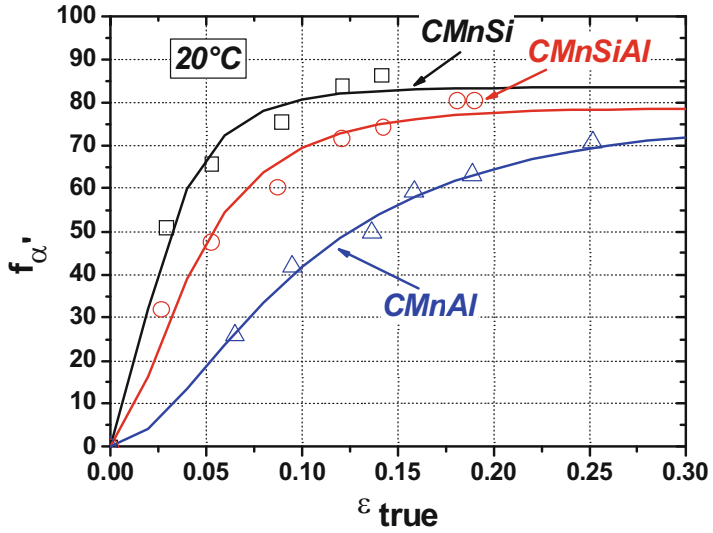

Fig. 4.11 Strain-induced martensite fraction ($f_{\alpha'}$) as a function of true strain (ε_{true}) for 0.24C-1.61Mn-1.45Si (CMnSi), 0.25C-1.70Mn-0.55Si-0.69Al (CMnSiAl), and 0.22C-1.68Mn-1.49Al (CMnAl) steels, plotted from data in [28]. Steel chemistries are in wt pct

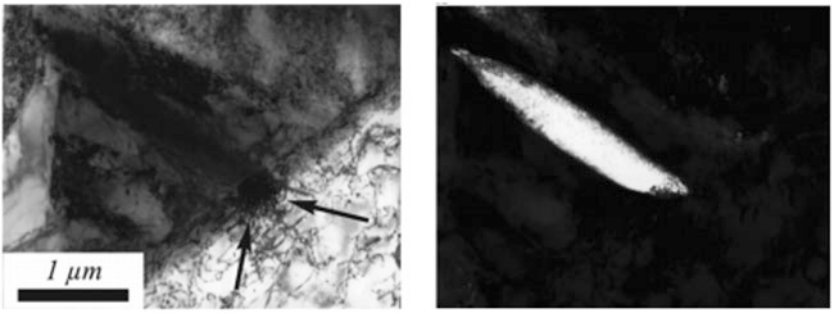

Fig. 4.12 (**a**) Bright-field and (**b**) dark-field TEM micrographs of a mechanical partially transformed austenite grain in a TRIP steel. Dark-field reflection taken from a martensite spot to illuminate the strain-induced martensite. From [30]

where $f_{\alpha'}$ is the fraction of martensite; α, β, and n are fitting parameters with α related to the generation of nucleation sites; β relates to the driving force for the $\gamma \rightarrow \alpha_M$ transformation; and n is a stereological parameter. Figure 4.12 shows micrographs of a TRIP steel following deformation with Fig. 4.12a showing a bright field TEM micrograph and Fig. 4.12b a corresponding dark field micrograph where reflection from a martensite/ferrite spot was used to illuminate the strain-induced martensite formed within the austenite [30]. It can further be noted that dislocations

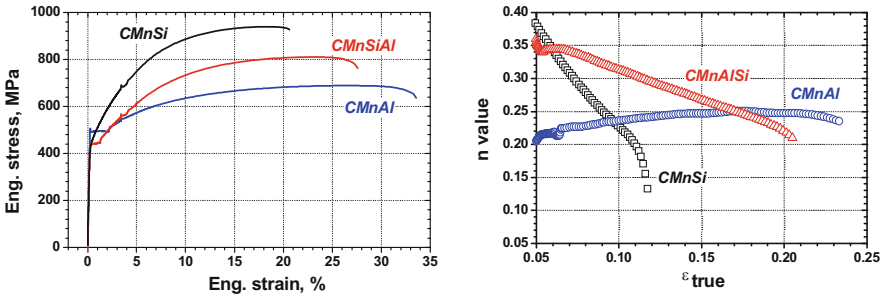

Fig. 4.13 (**a**) Engineering stress-strain curves and (**b**) corresponding instantaneous strain hardening (n-value) as a function of true strain for 0.24C-1.61Mn-1.45Si (CMnSi), 0.25C-1.70Mn-0.55Si-0.69Al (CMnSiAl), and 0.22C-1.68Mn-1.49Al (CMnAl) steels [31]. Steel chemistries are in wt pct

were generated at the strain-induced martensite/ferrite boundary in the ferrite. These dislocations help to harden the steel and improve strain hardening. Engineering stress-strain curves and corresponding instantaneous strain hardening (n-value) are shown from three TRIP steels in Fig. 4.13 [31]. Note that the corresponding retained austenite evolution with strain was presented in Fig. 4.11 for these steels. The degree of improved strain hardening is dependent on the austenite stability as reflected by comparing Figs. 4.13 and 4.11. It can be seen that the austenite in the CMnSi steel shows the least stability, i.e., the greatest rate of martensite formation with strain (Fig. 4.11) resulting in a continuously decreasing rate of strain hardening (Fig. 4.13). The CMnAl steel exhibits the slowest transformation with strain, i.e., greatest mechanical stability, and results in n-values increasing with strain up to high levels that postpone necking to greater levels of strain, and the highest uniform elongation is observed for this steel compared to the other steels. The CMnSiAl alloy exhibits intermediate mechanical stability of the austenite and strain hardening.

In addition to the M_s temperature as a measure for the thermal stability of the austenite against transformation to martensite, the M_S^σ, M_d^{30}, and M_d temperatures have been introduced [32–36] to assess the mechanical stability of the austenite against transformation upon mechanical loading. A schematic of stress required for austenite to martensite transformation to occur as a function of temperature situating these various temperature parameters is shown in Fig. 4.14 [37]. Undercooling below the M_s temperature is sufficient to induce martensite transformation without the application of load or requiring deformation to transform the austenite. At temperatures above the M_s temperature, the austenite may be transformed by loading the material. If transformation occurs prior to the yielding of austenite, the transformation is stress assisted, and increased stress levels are required with increasing testing temperatures. At greater temperatures, yielding of the austenite will occur prior to martensite formation, and the transformation is referred to as strain induced. The M_S^σ temperature delineates the stress-assisted from the

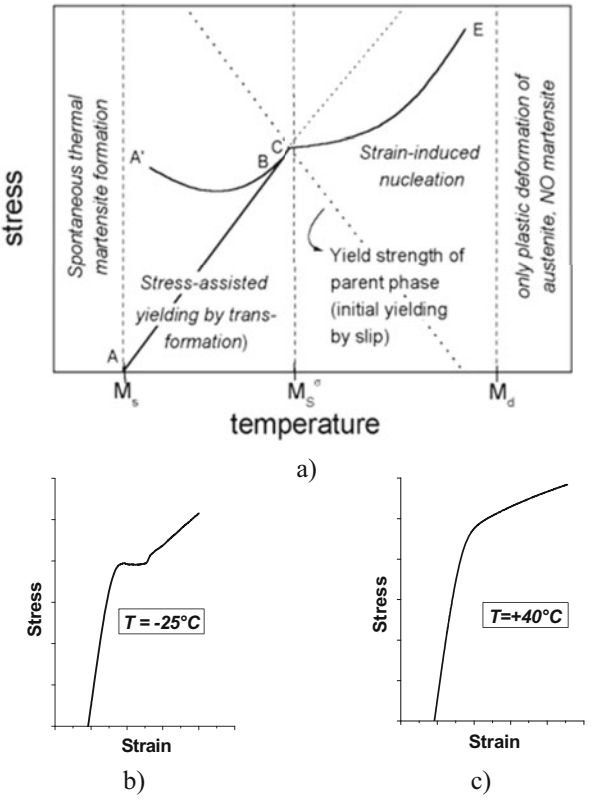

Fig. 4.14 Schematic representation of (**a**) stress required for transformation to occur as a function of temperature where the M_S, M_S^σ, and M_d temperatures are identified [37], (**b**) engineering stress-strain curve when stress-assisted transformation occurs, and (**c**) yielding associated with strain-induced transformation [31]

strain-induced transformation temperature range. Stress-assisted transformation of austenite into martensite occurs upon applying stress, and martensite nucleates on preexisting nucleation sites; transformation occurs prior to plastic deformation and yielding of the austenite. Increased stress levels are required for transformation with temperature at which the material is loaded. Strain-induced transformation is preceded by yielding of the austenite and the generation of nucleation sites for martensite. The M_S^σ temperature corresponds to the deformation temperature where the yield strength of the austenite equals the required stress for transformation to occur. If the steel is loaded at temperatures greater than the M_S^σ temperature, the stress required to induce austenite transformation exceeds the yield strength of the austenite, and, therefore, plastic deformation of the austenite occurs prior to transformation. Increased stress levels for transformation are again required with increasing testing temperature albeit a nonlinear relationship between the required stress and temperature developing. The transition from stress-assisted to strain-induced transformation is characterized by a change in yielding behavior where a plateau is observed in the stress-assisted transformation temperature regime below M_S^σ and round-house yielding at temperatures exceeding M_S^σ as illustrated in Fig. 4.14. The plateau in the stress-strain curves directly relates to the transformation

from austenite into martensite, which is associated with a sudden volume increase. The difference in yielding behavior enables determining the M_S^{σ} temperature experimentally using the single-specimen temperature-variable tension test (SS-TV-TT) [33, 34]. At a certain temperature, referred to as M_d, no transformation of austenite occurs, and only plastic deformation exists. An intermediate temperature, the so-called M_d^{30} temperature, has been defined as the temperature at which 50 pct of the originally present, i.e., in the unstrained condition, austenite volume fraction will transform to martensite at an applied strain of 30 pct. The M_d^{30} temperature is a measure of the overall austenite stability where a high M_d^{30} temperature is related to low mechanical stability of the austenite and has been shown to be related to the chemical composition of the austenite, in particular, carbon content and overall TRIP steel chemistry [28].

As vehicles in service may experience deformation at high strain rates (~102/s) during, e.g., vehicle collisions, it is important to assess tensile properties at strain rates far exceeding typical quasi-static strain rates employed in tensile tests (on the order of $10^{-}4$/s). These strain rates are so elevated that insufficient time is available for heat dissipation and adiabatic heating may occur. The austenite transformation is susceptible to relatively small changes in temperature, and adiabatic heating of the steel results in reduced transformation behavior, i.e., greater austenite stability. This in turn affects the dynamic stress-strain behavior and amount of energy absorbed during a crash. A comparison of energy absorption during dynamic testing as a function of dynamic tensile strength for a variety of steel grades is shown in Fig. 4.15 [38]. The energy values were obtained by assessing the surface area under dynamic stress-strain curves generated on a split-Hopkinson bar test in tension [38, 39]. TRIP steels show superior behavior compared to structural, low-carbon (low C),

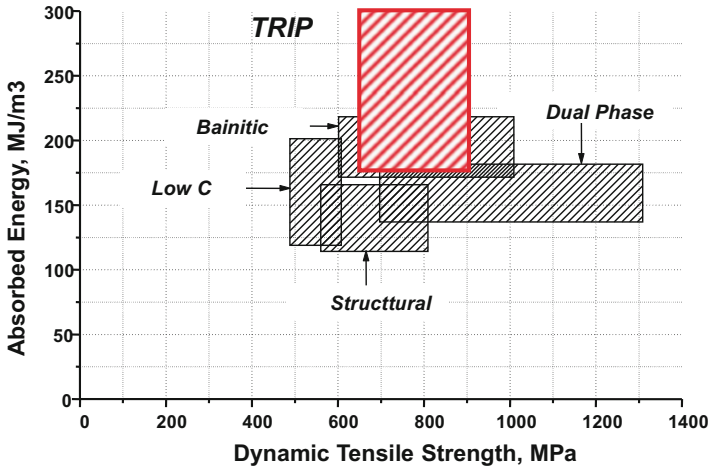

Fig. 4.15 Absorbed energy under dynamic loading situating TRIP steel performance with respect to structural, low-carbon (low C), and dual-phase steels [38]

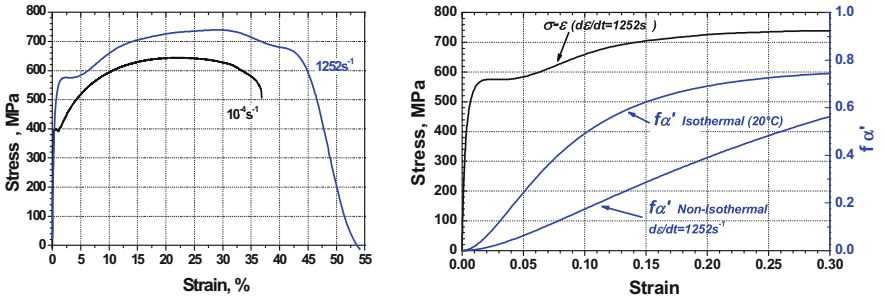

Fig. 4.16 (**a**) Engineering stress-strain curves obtained by testing at a quasi-static strain rate of 10^{-4}/s and dynamic at 1252/s by split-Hopkinson bar testing in tension, (**b**) strain-induced transformation as a function of strain for isothermal testing at room temperature and calculated effect of adiabatic heating during dynamic testing on martensite evolution superimposed on the dynamic stress-strain curve shown in (**a**) [40]

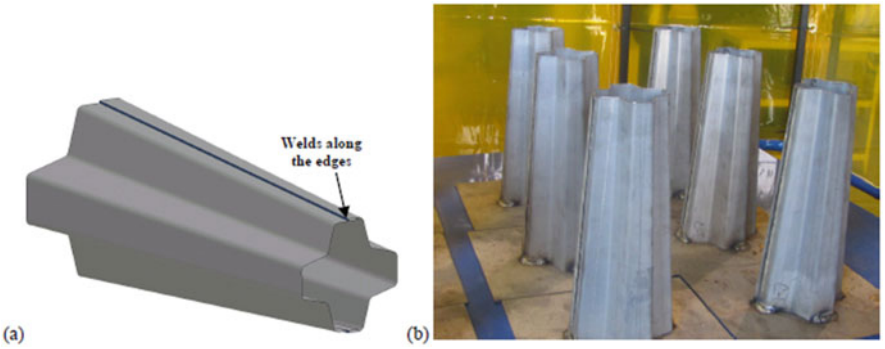

Fig. 4.17 (**a**) Schematic of a 12-sided component for drop-weight testing, and (**b**) welded components prior to testing [41]

bainitic, and DP steels. Examples of engineering stress-strain curves under quasi-static and dynamic testing are shown in Fig. 4.16a [40]. Superior strength levels, elongation, and absorbed energy develop under dynamic loading. Figure 4.16b shows the calculated effect of adiabatic heating on the strain-induced martensite evolution with strain during dynamic loading. Reduced kinetics are clearly observed compared to the martensite evolution at room temperature, and these reduced kinetics are believed to be involved in the superior dynamic energy absorption by TRIP steels as shown in Fig. 4.15.

In addition to dynamic tensile properties, components may be tested to assess crashworthiness and enable comparison of steel grade performance for crumple zone applications. To this end, components may be tested as shown in Fig. 4.17 [41] in a drop tower apparatus where a weight is dropped from a prescribed height and the reduction in height after axial crash testing is assessed. Photographs of the

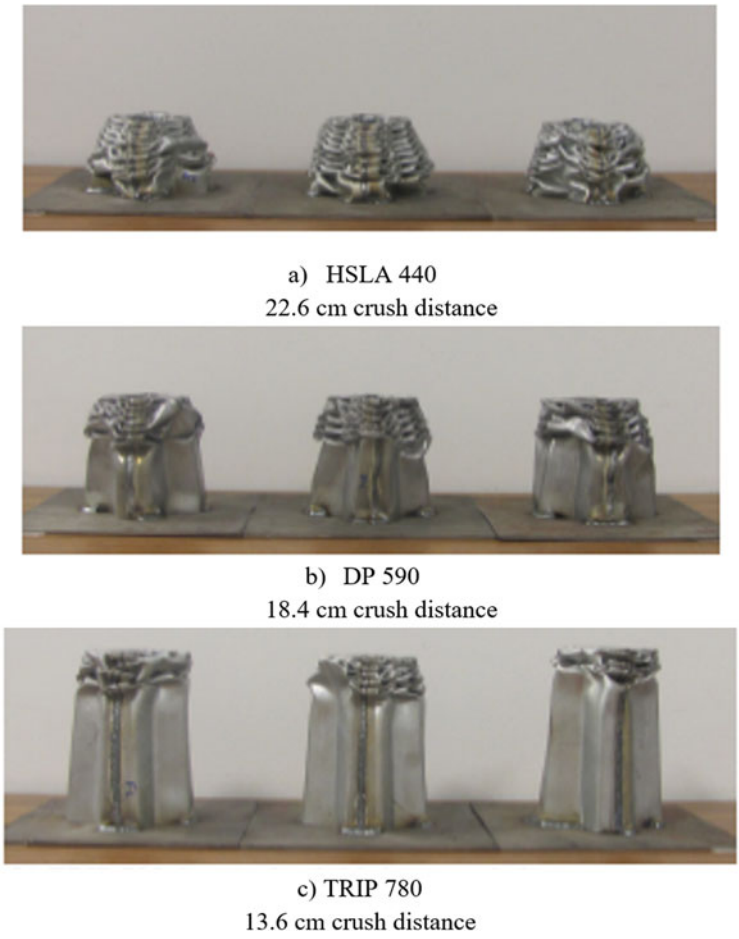

Fig. 4.18 Components after crash testing showing the response of (**a**) HSLA 440, (**b**) DP 590, and (**c**) TRIP 780 [41]. The crush distances representing the height difference between the component prior and after crash testing are also shown. (Adapted from [41])

components following interaction with the weight are shown in Fig. 4.18 where various steel grades are compared namely HSLA, DP, and TRIP steels at a variety of strength levels. The crush distance, i.e., the difference between the height of the component prior to impact and after impact, is also indicated where the lower strength HSLA material shows the greatest compaction following the weight drop, followed by DP and TRIP steels. Further analysis of this test can include assessment of crack formation in the crushed component.

4.4 TRIP-Bainitic Ferrite Steels

A further development from low-carbon TRIP steels are the so-called TRIP-bainitic ferrite (TBF) steels which again rely on the TRIP effect for improved work hardening and tensile elongation at strength levels exceeding typical levels observed for low-carbon TRIP steels. The difference in strength results from reduced or absent intercritical ferrite volume fractions. A heat-treating schematic for TBF steels is shown in Fig. 4.19, where reheating following cold rolling is in the fully austenitic rather than the intercritical region [42]. The reheating step is followed by isothermal holding and quenching to room temperature. The isothermal hold can be done at a variety of temperatures and results in austempering or the introduction of some initial martensite (depending on the temperature) followed by further austenite decomposition in low-temperature transformation products. TRIP steel compositions are suited for TBF processing, and retained austenite is present in resulting microstructures stabilized by carbon enrichment resulting predominantly from a bainitic transformation. TBF steels show attractive properties as shown in Fig. 4.20 which plots tensile properties as a function of holding temperature (referred to as annealing temperature, T_A, in Fig. 4.19) for a fixed holding time of 200 s. Increased strength levels evolve with lower holding temperatures along with reduced total and uniform elongation. TBF steels are attractive third-generation AHSS as evident from their mechanical properties.

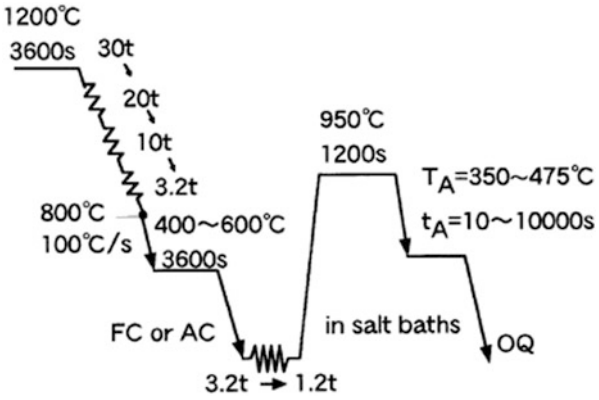

Fig. 4.19 Processing schematic detailing hot rolling, cold rolling, and annealing for a 0.20C-1.51Si-1.51Mn (wt pct) TBF steel [42]

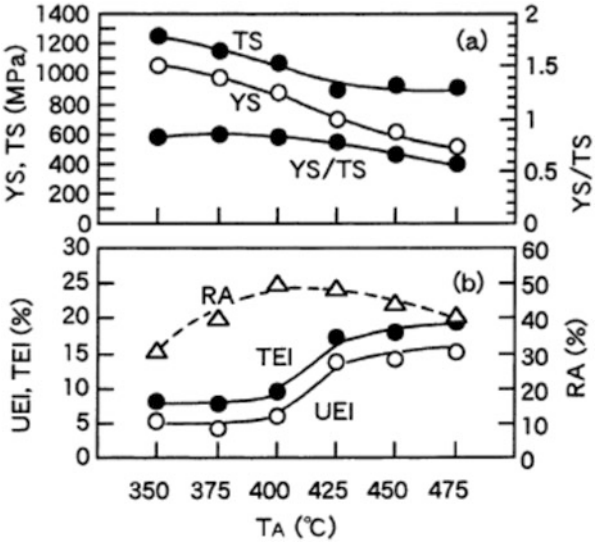

Fig. 4.20 Yield strength (YS), tensile strength (TS), their ratio (YS/TS), uniform (UEl), and total elongation (TEl) reduction in area (RA) as a function of isothermal annealing temperature (T_A) shown in Fig. 4.19 and a holding time of 200 s [42]

4.5 Quenching and Partitioning Steels

Another important family of third-generation AHSS constitutes the quenching and partitioning (Q&P) steels [43–45]. Q&P steels have a martensitic microstructure containing film-like retained austenite. Intercritical ferrite may also be present. A heat-treating and microstructural evolution schematic of Q&P is provided in Fig. 4.21. Reheating can be performed in the intercritical region or result in full austenitization as shown in the schematic and is followed by quenching at a temperature intermediate between the martensite start and finish temperatures. At this so-called quenching temperature (QT), the microstructure consists of martensite and any remaining austenite. The latter phase is stabilized by carbon enrichment during a secondary step at the same or a higher temperature. This secondary heat-treating step is referred to as the partitioning step, which aims at carbon enrichment of austenite by carbon transfer from the martensitic matrix. Quenching to room temperature may result in some additional martensite formation depending on the level of austenite stabilization and carbon enrichment.

Example micrographs of Q&P microstructures are shown in Fig. 4.22 [47, 48]. The microstructure consists of fine martensitic laths with a high dislocation density and austenite with a film-like appearance, separating the martensite laths as shown in the dark-field TEM micrograph in Fig. 4.22b illuminated using an austenite reflection. The bright-field image included in Fig. 4.22c clearly also shows transition carbides present. Quantitative analysis using Mössbauer spectroscopy

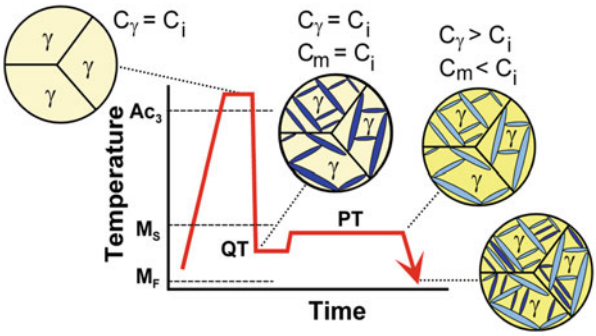

Fig. 4.21 Schematic illustrating the quenching and partitioning heat-treating process. QT is the quenching temperature, PT is the partitioning temperature and M_s and M_f are the martensite start and finish temperatures, respectively. C_i, C_γ, and C_m refer to the carbon contents of the initial alloy, austenite, and martensite, respectively [46]

[49] has indicated that lower levels of η transition carbides are observed in Q&P versus quench and tempered (Q&T) steels for the same partitioning/tempering conditions. This indicates that carbon supersaturation of martensite is relieved by carbide formation in Q&T steels whereas carbon transport to austenite and its resulting retention are predominantly operating in Q&P steels. Retained austenite levels superior to levels obtained following Q&T were also observed in this study [49]. These results suggest that both carbon partitioning from martensite into austenite and carbide precipitation are active mechanisms toward alleviating carbon supersaturation of martensite.

The effect of the quenching temperature (QT) on the fraction of austenite that can be retained assuming full carbon depletion of martensite and enrichment into the austenite is shown in Fig. 4.23. A maximum fraction is obtained for an "optimal" QT. This optimum QT is obtained by considering the fraction of martensite forming as a function of the offset with the M_s temperature and the carbon available in the formed martensite. Assumption of full carbon depletion of the martensite or "idealized" partitioning enables determination of the optimum QT and corresponding fraction [50]. Further details on the methodology and calculation can be found in [50].

Example engineering stress-strain curves are shown in Fig. 4.24 for a 0.3C-3Mn-1.6Si (wt pct) alloy processed by Q&P heat treating following full austenitization. It should be noted that this alloy chemistry is richer than traditional TRIP steel chemistries. The latter have been employed extensively to study Q&P heat-treating responses as they are suited for Q&P processing given the presence of cementite retarding alloying elements such as Si. High ultimate tensile strength levels approximating 1500 MPa and total elongation over 16 pct are apparent in the engineering stress-strain curves shown in Fig. 4.24. The curves show round-house yielding with high yield strengths and substantial amounts of strain hardening.

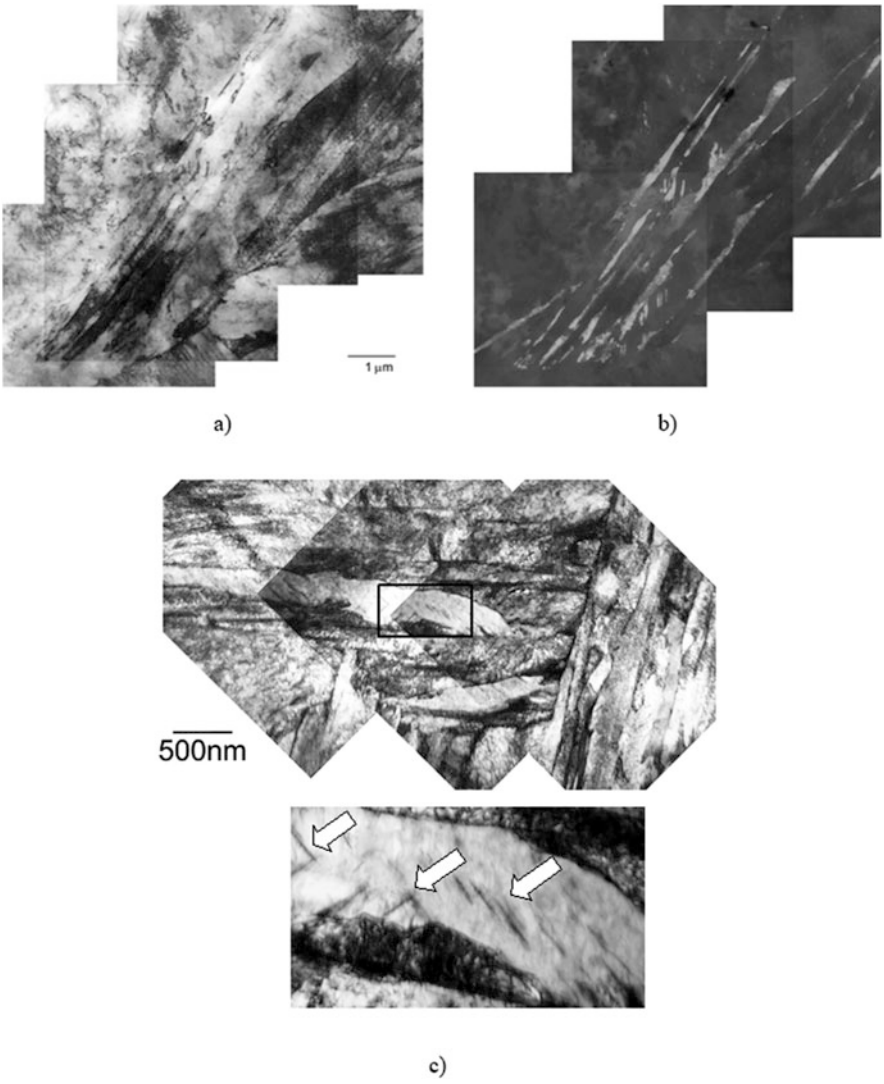

Fig. 4.22 TEM micrographs of Q&P microstructures of a Fe-0.20C-1.63Mn-1.63Si (wt pct) composition QT: 240 °C, PT: 400 °C, Pt: 120 s. (**a**) Bright-field and (**b**) dark-field images taken using an austenite reflection, (**c**) bright-field image of a Q&P microstructure showing the presence of transition carbides (QT: 240 °C, PT: 300 °C, Pt: 120 s) [47, 48]. *QT* quenching temperature, *PT* partitioning temperature, *Pt* partitioning time

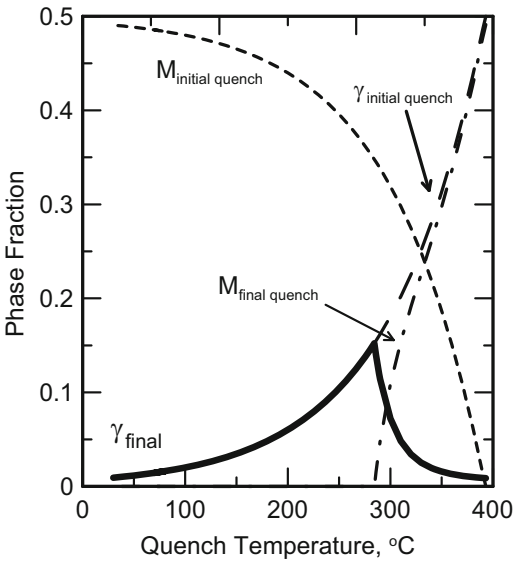

Fig. 4.23 Predicted phase fractions for a 0.19C steel containing 50 vol pct intercritical ferrite versus quenching temperature. The austenite fraction following Q&P heat treating and assuming "idealized" partitioning is shown in bold as γ_{final}. The initial martensite fraction is shown based on the Koistinen-Marburger equation as $M_{initial\ quench}$ and corresponding remaining austenite at this stage as $\gamma_{initial\ quench}$. The martensite forming during final quenching due to insufficient carbon stabilization is shown as $M_{final\ quench}$ [50]

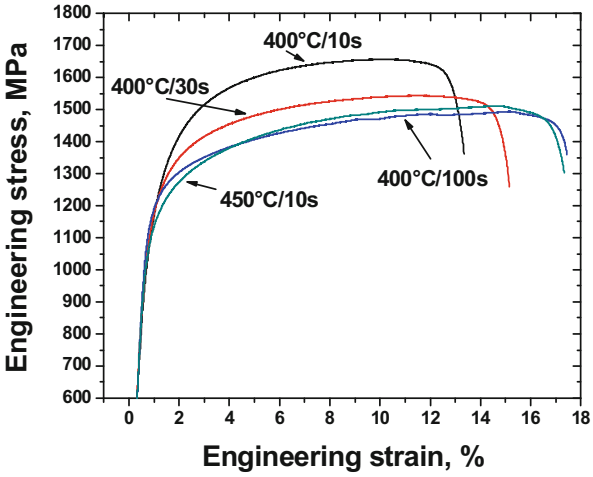

Fig. 4.24 Engineering stress-strain curves obtained in Fe-0.3C-3Mn-1.6Si (wt pct) alloy Q&P heat treated following full austenitization using a quenching temperature of 200 °C and the indicated partitioning conditions [51]

4.6 Medium Manganese Steels

Another third-generation AHSS concept are the medium manganese steels typically containing 5–12 wt pct Mn and are based on a concept proposed by Miller [52]. The heat treating for these steels consists of reheating and holding in the intercritical region to establish fractions of ferrite and austenite and to stimulate diffusion of manganese (and carbon) solute from ferrite into austenite, thereby stabilizing it to room temperature. Depending on the effectiveness of the heat treatment, all of the austenite present at high temperature can be retained to room temperature.

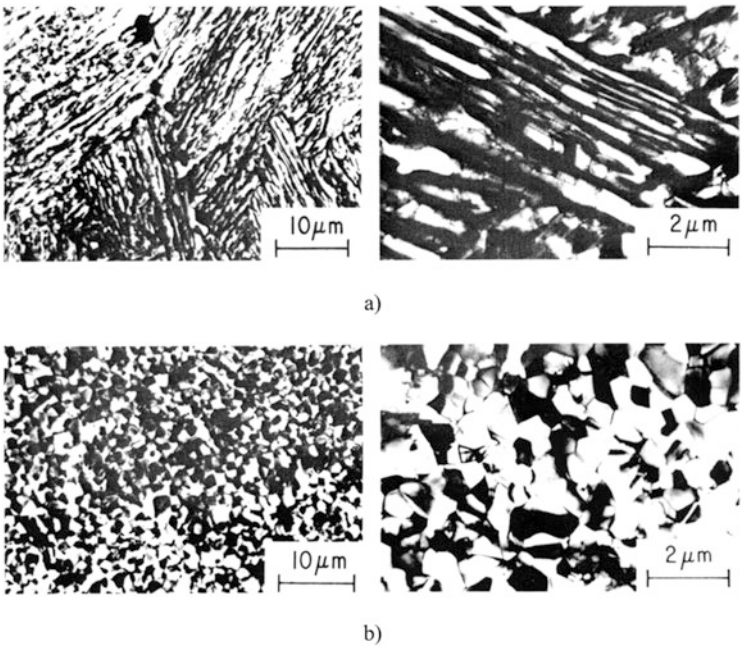

Fig. 4.25 TEM micrographs of a 0.11C-5.7Mn steel intercritically annealed at 600 °C for 1 hr. after (**a**) hot rolling, and (**b**) cold rolling [52]

An optimal intercritical annealing temperature can be calculated assuming full partitioning of solute between ferrite and austenite [53]. TEM micrographs of medium manganese steel microstructures are shown in Fig. 4.25 where intercritical annealing was done following hot rolling (Fig. 4.25a) and cold rolling (Fig. 4.25b), respectively, at a temperature of 600 °C for 1 h. Lath-like ferrite and austenite are apparent following the application of the intercritical heat treatment after hot rolling reminiscent of the martensitic hot band microstructure whereas equiaxed grains of ferrite and austenite develop following intercritical annealing of the cold rolled condition. Low dislocation densities in the ferrite are observed in both cases and far less than observed in a (cold-rolled) martensitic microstructure.

The intercritical annealing heat treatment has been explored using simulated and industrial batch annealing and continuous annealing. Thermal profiles shown in Fig. 4.26 representing batch annealing have been applied to enable effective intercritical annealing with solute partitioning approximating equilibrium levels [54]. More recently, cycles reflective of continuous annealing have been pursued, and austenite was effectively retained at room temperature resulting from solute enrichment as indicated by the TEM micrograph shown in Fig. 4.27 [55]. Energy-dispersive spectroscopy (EDS) analysis along a line scan on the micrograph clearly indicates manganese enrichment in the austenitic region following short time annealing of 180 s in the intercritical temperature range.

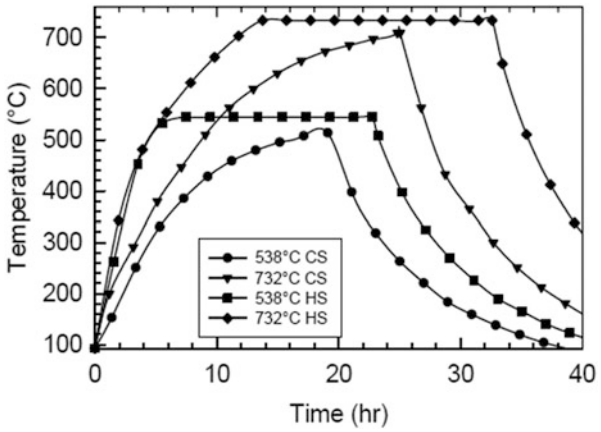

Fig. 4.26 Example annealing cycles employed in [54] to assess intercritical annealing of medium manganese steels using batch annealing. Cold-spot (CS) and hot-spot (HS) temperature-time evolution illustrated

Austenite amount and stability are important for tensile properties. Figure 4.28a shows the mechanical stability of retained austenite measured in a 0.1C-7Mn (wt pct) steel intercritically annealed for 1 week at a variety of temperatures [56]. Corresponding engineering stress-strain curves using the same color coding are included in Fig. 4.28b, and a family of stress-strain curves develops. Both mechanical stability of retained austenite and tensile behaviors are greatly dependent on the employed annealing temperature. The lowest intercritical annealing (IA) temperature of 575 °C shows a large yield point elongation (YPE) followed by limited strain hardening and intermediate elongation. At a higher IA temperature, the YPE decreases, and substantial strain hardening follows leading to very high elongation levels (e.g., 600 °C). IA at an even greater temperature of 675 °C results in a markedly different shape of the stress-strain curve where YPE is absent, yielding occurs at a much lower stress level, and very rapid strain hardening results in failure at much lower elongation levels. The corresponding retained austenite evolution with strain indicates that the mechanical stability of the austenite substantially impacts the stress-strain behavior, in particular, strain hardening where intermediate stability results in substantial strain hardening and high elongation levels. Low stability (e.g., at an IA of 650 °C) results in very pronounced strain hardening over a limited strain range resulting in the high ultimate tensile strength levels but low elongation levels.

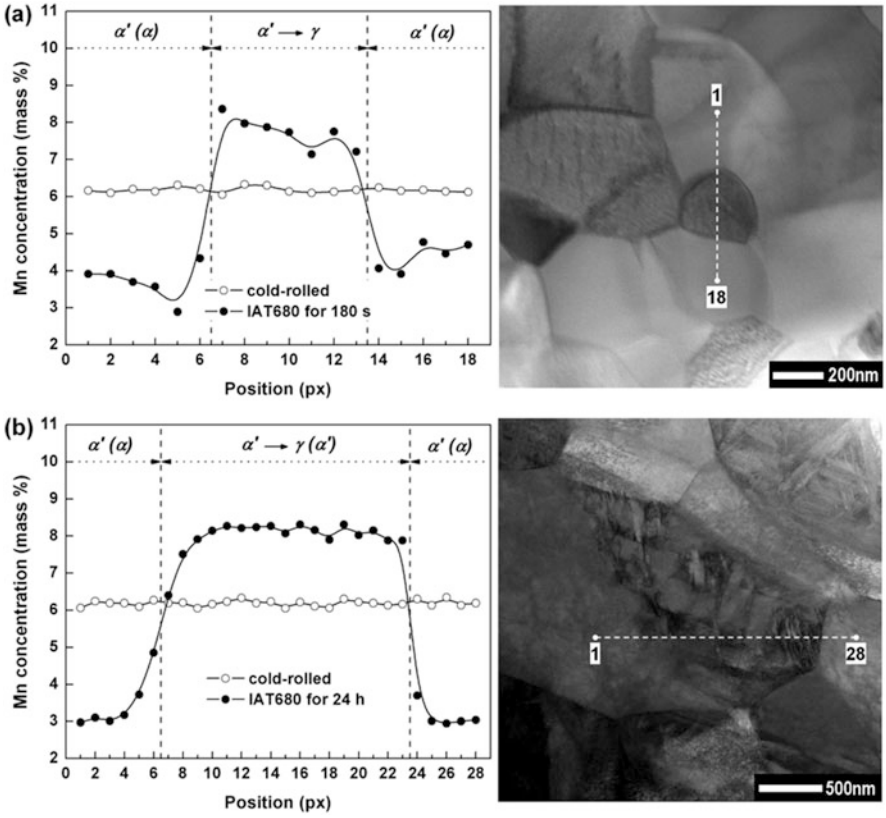

Fig. 4.27 EDS and TEM micrographs of a Fe-0.05C-6.15Mn-1.4Si-0.04Al (wt pct) steel intercritically annealed at 680 °C for (**a**) 180 s and (**b**) 24 hr. [55]

4.7 Press-Hardenable Steels

Another important industrial technology is press hardening or hot stamping that enables the manufacturing of high-strength martensitic components with complex geometries. An example BIW where press-hardenable steels (PHS) are widespread is shown in Fig. 4.29. A number of antiintrusion components such as door beams, pillars, etc., employ PHS steels. Press hardening circumvents the challenge of reduced ductility associated with higher strength levels by forming complex parts at high temperatures where high ductility exists in the austenitic phase field, followed by accelerated cooling in the dies to set the final, martensitic microstructure exhibiting high strength that will enhance vehicle performance in anti-intrusion components. Unlike the prior steels discussed, the properties of press-hardenable steels are set following shaping of the component. Hot stamping is particularly instrumental for components requiring the use of dies with tight radii that may

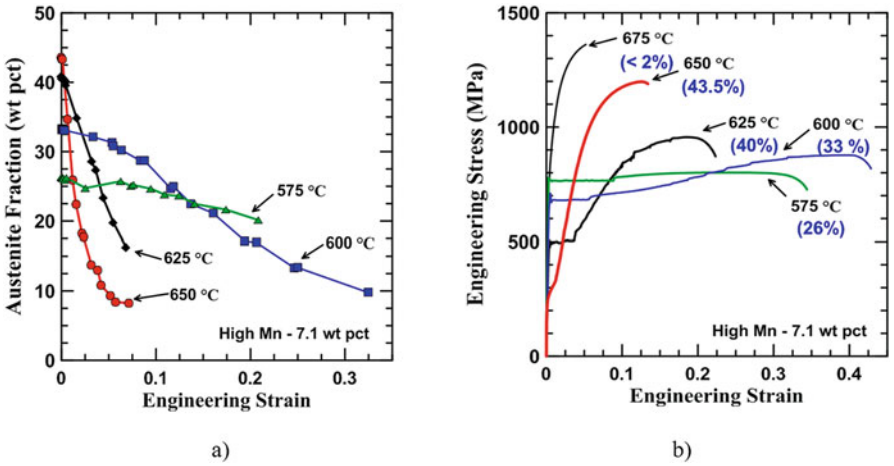

Fig. 4.28 Mechanical stability of retained austenite and tensile behavior of a 0.1C-7.1Mn (wt pct) steel intercritically annealed for 168 hours at various IA temperatures. (**a**) Austenite fraction as a function of engineering strain and (**b**) corresponding engineering stress-strain curves with initial austenite fractions (vol pct) indicated in brackets [56]

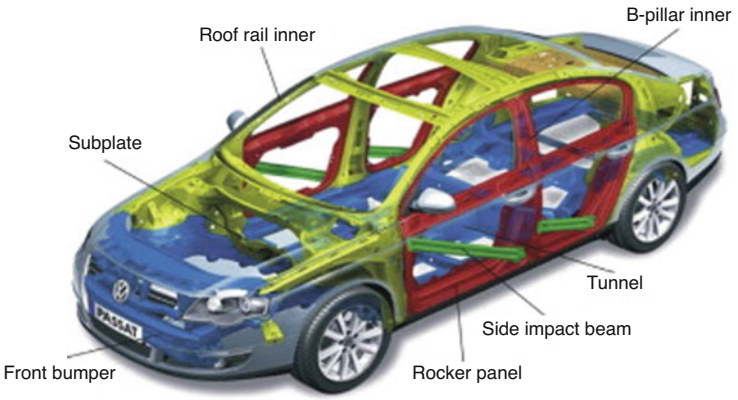

Fig. 4.29 BIW showing application of PHS steels in various locations [59]

induce failures at the edge of the die and where springback is of concern [57, 58]. PHS processing can be done with cooling taking place immediately following forming using the same die sets that remain closed to accelerate cool the part following sheet forming. Alternately, it can be done in two steps where forming is done in one set of dies, and the formed component is transferred to a secondary die set which will cool the part and where the final microstructure will be set. Schematics of both processing routes are shown in Fig. 4.30 and are referred to as direct and indirect press hardening, respectively [59].

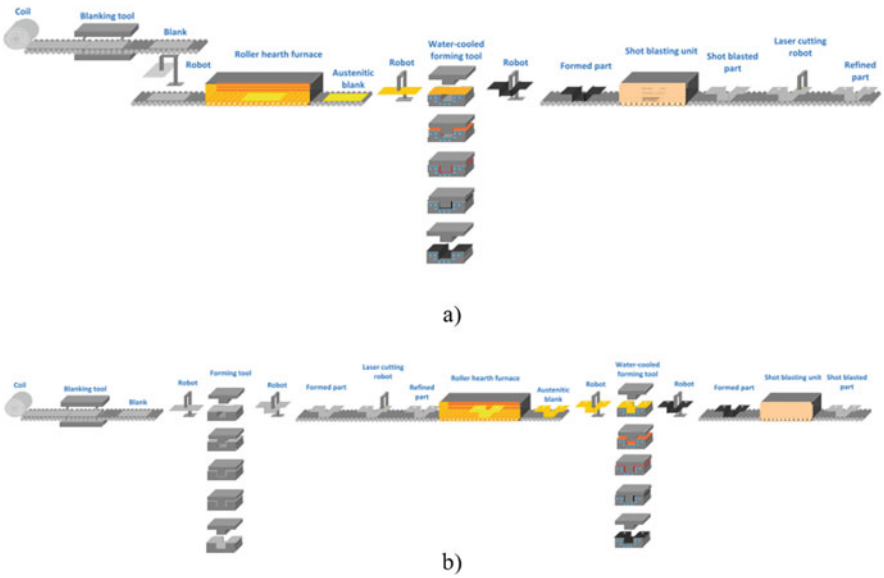

Fig. 4.30 Schematic of the hot stamping processing: (**a**) direct and (**b**) indirect [59]

In order to establish a fully martensitic high-strength microstructure, hardenability needs to be compatible with cooling rates obtained by quenching in water-cooled dies. To this end, alloying with boron is widespread, and the boron is protected from interaction with nitrogen by tying up the nitrogen into a more stable nitride such as a titanium nitride. Solute boron will segregate to prior austenite grain boundaries and poison nucleation sites for nonmartensitic transformation products. A common alloy is referred to as 22MnB5 with example chemical composition range 0.20–0.25C,1.10–1.40Mn,0.15–0.35Si,0.15–0.35Cr,0.02–0.05Ti,0.002–0.005B (wt pct) [59]. A representative continuous cooling transformation (CCT) diagram for 22MnB5 is shown in Fig. 4.31 [60, 61]. From the CCT diagram, it can be shown that the cooling rate must exceed 27 °C/s to avoid ferritic and/or bainitic transformation products.

4.8 TWIP Steels

Second-generation AHSS employ greater levels of alloying to stabilize an austenitic microstructure. As shown in Fig. 4.1, stainless steels properties fall in the same band as the second-generation AHSS properties envelope. Twinning-induced plasticity (TWIP) steels are also second-generation AHSS with a fully austenitic microstructure stabilized by additions of manganese and carbon to substitute for more expensive nickel [13, 62–68]. Engineering stress-strain curves for TWIP steels

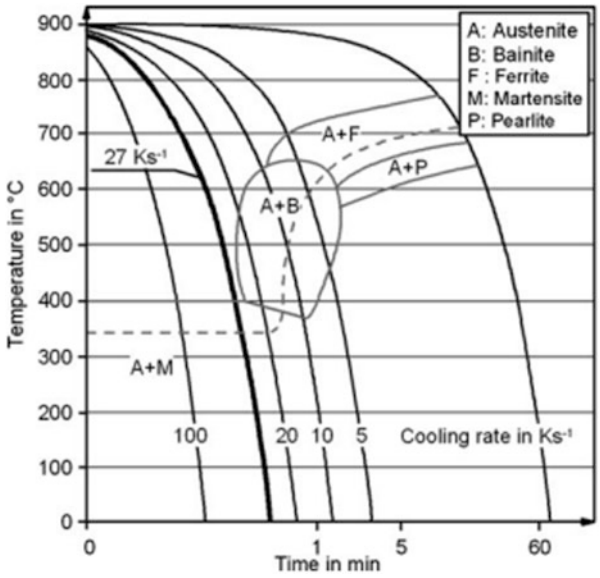

Fig. 4.31 Continuous cooling transformation diagram for 22MnB5 grade [60, 61]

are compared to first-generation AHSS, a low-carbon (low C) steel with a ferrite-pearlite microstructure, and a fully martensitic (M220) steel in Fig. 4.32 [69]. Very pronounced strain hardening results in very high tensile elongation, and the exhibited tensile properties are exceptional when compared to leaner compositions. The TWIP steels exhibit ultimate tensile strengths of approximately 1000 MPa. It should be noted that relatively low yield strengths are observed especially compared to yield strengths exhibited by third-generation AHSS such as Q&P steels. Example TWIP steel compositions are shown in Table 4.1. Heat treating following cold rolling consists of annealing to recrystallize the austenitic microstructure and set the final grain size [70, 71].

The stacking fault energy (SFE) is a critical parameter governing the stress-strain behavior, tensile properties, and strain hardening of TWIP steels. Ranges for the intrinsic stacking fault energy for various TWIP steel alloying concepts and associated deformation mechanisms, such as phase transformations, deformation twinning, and dislocation glide and cell formation, are shown in Fig. 4.33 [13, 82–85].

Transmission electron micrographs of deformed TWIP steels are shown in Fig. 4.34 [86] where dislocation cell-like structures develop in a Fe-30Mn (wt pct) steel whereas extensive twinning is observed in a Fe-22Mn-0.6C (wt pct) alloy, and the latter steel exhibits superior strain hardening and tensile behavior resulting from mechanical twin formation [86].

As shown in Fig. 4.33, phase transformations may occur depending on alloying and associated stacking fault energy. An example of α' martensite nucleated at the

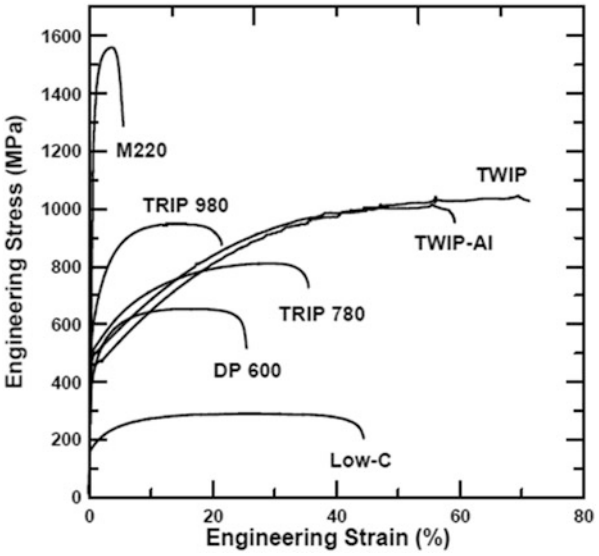

Fig. 4.32 Comparison of engineering stress-strain curves of first-generation AHSS DP and TRIP steels: a low-carbon (low-C) mild steel, a fully martensitic M220, and two TWIP steels [69]

Table 4.1 Example TWIP steel compositions

wt pct	Ref.
Fe-(18–24)Mn-(0.5–0.7)C	[72, 73]
Fe-18Mn-0.6C-(1.5–2.5)Al	[13, 74]
Fe-(15–27)Mn-(0.4–0.7)C-(1.3–3.5)Al-(0–3)Si	[75–80]
Fe-(17–22)Mn-(0.45–0.60)C-(0.1–0.3)V	[13, 81]
Fe-22Mn-0.6C-(0.1–0.3)Ti	[81]
Fe-18Mn-0.6C-0.31Nb	[81]

intersection of two ε martensite bands in a Fe–18Mn–0.25C–0.084 N (wt pct) alloy is shown in Fig. 4.35 [87].

The exploitation of phase transformations in high manganese steels has led to the investigation of TRIP/TWIP alloys [62]. Figure 4.36 shows the tensile response of Fe-xMn-3Al-3Si (wt pct) alloys with varying Mn contents ranging from 15 over 20 to 25 wt pct [62]. Reduced Mn alloying results in an inflection in the stress-strain curves associated with the activation of abundant austenite transformation. The Mn content of the alloy exhibiting this behavior is leaner than typical TWIP steel compositions.

TWIP steels have seen fairly limited application to date as the rich alloying to stabilize the austenite makes their widespread implementation cost prohibitive. Furthermore, the application of TWIP steels has been hindered in the past due to sensitivity to hydrogen embrittlement [88–90] observed following, e.g., cup drawing tests as illustrated in Fig. 4.37 [91] albeit this embrittlement sensitivity is not necessarily revealed during tensile testing in hydrogen charged specimens [69, 92].

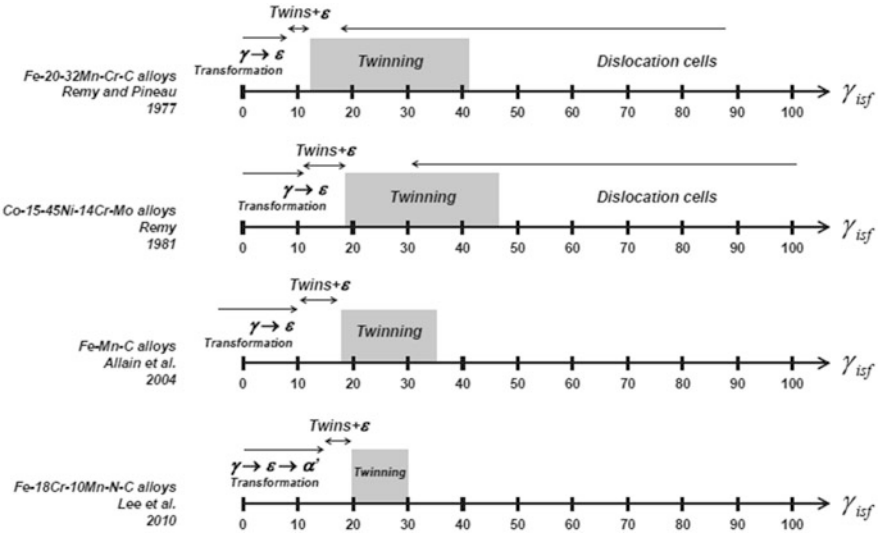

Fig. 4.33 Overview of ranges of intrinsic stacking fault energies for phase transformation, deformation twinning, and dislocation glide in austenitic Fe-(20–32)Mn-Cr-C alloys, Co-(15–45)Ni-14Cr-Mo alloys, Fe-Mn-C TWIP steels, and Fe-18Cr-10Ni-C-N alloys [13]. Based on data compiled from Remy and Pineau [82], Remy [83], Allain et al. [84] and Lee et al. [85]. (Elemental concentrations are in wt pct)

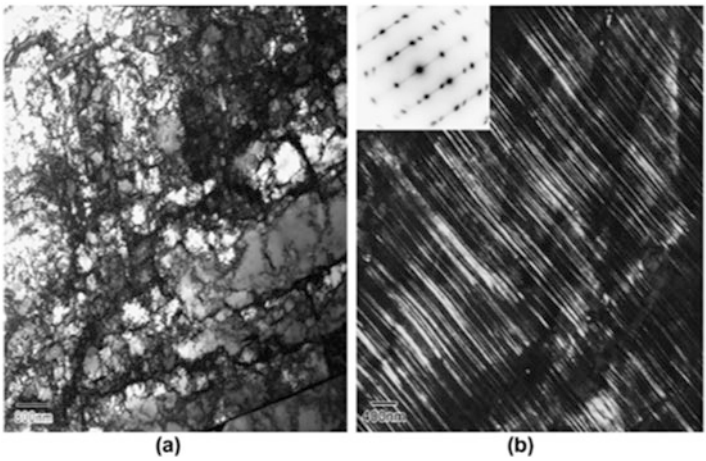

Fig. 4.34 TEM micrographs showing (**a**) a bright-field image showing well-developed dislocation cell-like structures in a Fe-30Mn (wt pct) steel deformed up to 20 pct in tension and (**b**) a dark-field image of a Fe-22Mn-0.6C (wt pct) deformed to 50 pct showing extensive mechanical twinning [86]

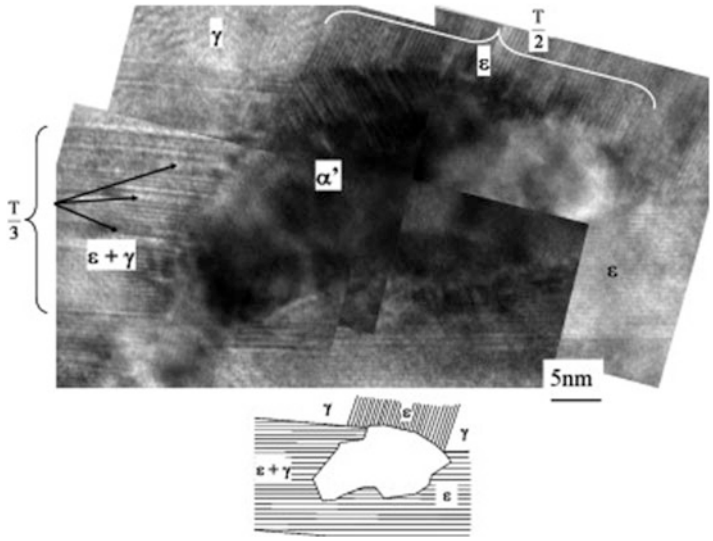

Fig. 4.35 α'martensite formed on the intersection of two ε martensite bands in a Fe–18Mn–0.25C–0.084 N (wt pct) alloy [87]

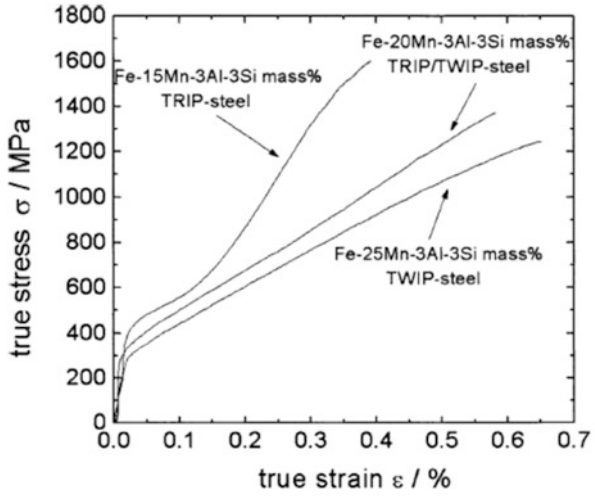

Fig. 4.36 True stress versus true strain curves showing the effect of Mn content in Fe-(15–25)Mn-3Al-3Si (wt pct) alloys [62]

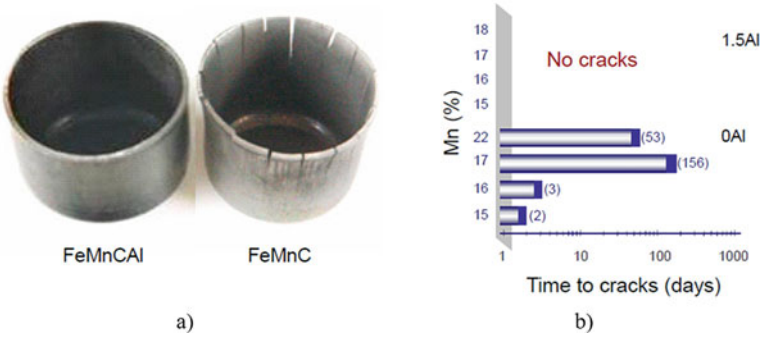

Fig. 4.37 (**a**) Delayed cracking observed following cup drawing in a Fe-Mn-C TWIP steel but not in a Fe-Mn-C-Al composition. (**b**) Time to cracks in days as a function of Mn and Al alloying [91]

Alloying with aluminum has alleviated this concern [91, 93], which is believed to be related to the suppression of ε martensite formation and due to stacking fault energy increases and reduced H segregation to mechanical twin interfaces and ε martensite [94, 95]. Figure 4.37 shows the absence of (delayed) cracking in a 1.5 wt pct Al-added TWIP steel following cup drawing.

4.9 Low-Density Steels

In order to further reduce the weight of AHSS, low-density steels are being explored that incorporate high levels of aluminum alloying in the range of 5–13 wt pct to reduce the density of steel and increase the specific strength (strength/weight ratio) [96–99]. Figure 4.38 shows the measured density of binary Fe-Al alloys as a function of Al content where a clear density reduction develops with increased Al levels [100]. Al additions have been explored in high and medium manganese ferritic, austenitic, and multiphase steels. Intermetallic formation such as Fe_3Al and FeAl has been observed to negatively impact ductility in the Fe-Al binary system, and, therefore, Al levels have typically been restricted to 10 wt pct [101, 102]. Al additions to Fe-Mn-C alloys have been studied extensively, and $(Fe,Mn)_3AlC$ carbide referred to as κ carbide develops in these alloys [101]. A summary of tensile properties of low-density steels is provided in Fig. 4.39 on an ultimate tensile strength versus total elongation diagram [96]. To date low-density steels have not seen significant application in automotive architectures.

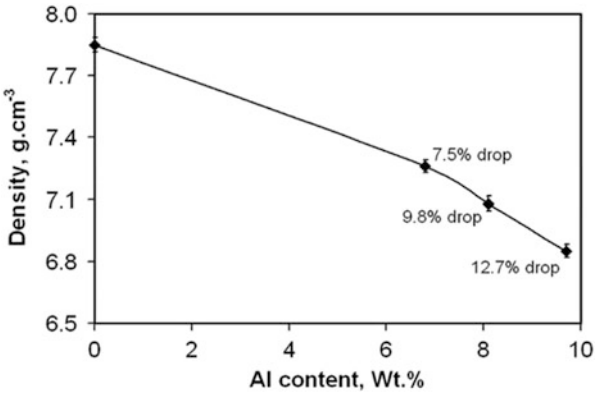

Fig. 4.38 Experimentally measured density as a function of Al content in binary Fe-Al alloys [100]

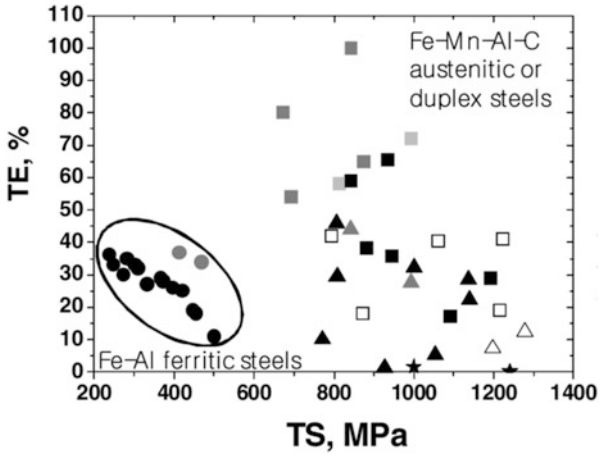

Fig. 4.39 Tensile total elongation (TE) as a function of tensile strength (TS) for various low-density steels [96]

4.10 Local Formability

The above sections have reviewed various AHSS automotive steel grades with particular emphasis on alloying, microstructure, and resulting tensile properties – an initial measure for global formability. Tensile properties measured at strain rates from quasistatic to dynamic are important in vehicle design and performance simulations and help predict achievable lightweighting levels. In order to enable implementation of these steel grades in vehicle architectures, further properties relevant to component manufacturing and in service performance assessment are required. These include formability testing, spring back, bending under tension

Fig. 4.40 Cracks observed in formed parts initiated at sheared edges [103]

testing, fatigue performance, bake hardening, and liquid metal and hydrogen embrittlement. A detailed review of these various aspects is beyond the scope of this chapter, and the discussion will be limited here to hole expansion testing or stretch flangeability, a measure for "local" formability. Examples of failed parts where cracks initiated at sheared edges are shown in Fig. 4.40 [103, 104].

In order to study shear edge stretching or stretch flangeability, the hole expansion test has been developed. The test consists of preparing a circular hole in a steel sheet by punching, and the hole is then expanded over a flat or conical die. The diameter expansion is measured following development of a through thickness crack. Manual measurements and automated camera systems are being used to measure the expansion. A schematic of the hole expansion test and samples expanded to failure are shown in Fig. 4.41 [105, 106]. A summary of hole expansion ratios (HER) defined as the percentage expansion of the initial diameter to failure is shown in Fig. 4.42a [107, 108]. In general, decreasing HER or reduced "local" formability is observed with increased ultimate tensile strength for most steel grades except for DP steels that deviate from the relationship developed for a variety of predominantly single-phase steel microstructures. Figure 4.42b shows the hole expansion ratio of DP steels as a function of ferrite content present in the microstructure, and an overall decreasing trend is apparent whereas uniform elongation increases with ferrite content [109]. Furthermore, it has been shown that, in general, HER increases with a reduced hardness ratio between the hardness of the martensite over the ferrite hardness [110].

The effect of the shearing process prior to forming is important and can be assessed by measuring the shear affected zone (SAZ), which is the material adjacent the sheared face work hardened during shearing [111, 112]. The degree of work hardening during shearing and, therefore, also the size of the SAZ relates to the degree of work hardening exhibited by the steel during tensile testing.

4.11 Summary

This chapter provides an overview of various advanced high-strength steels for structural applications in vehicle architectures. These AHSS enable lightweighting of vehicles via down gauging of steel components. Various families of AHSS exist

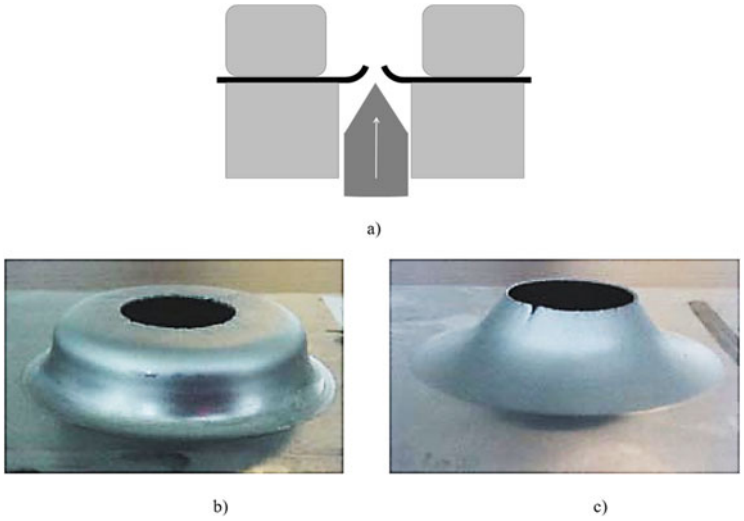

Fig. 4.41 (**a**) Schematic of hole expansion test showing the punched and expanded sample (black) and the conical die expanding the sample, and samples expanded to failure using (**b**) a flat die and (**c**) a conical die [105, 106]

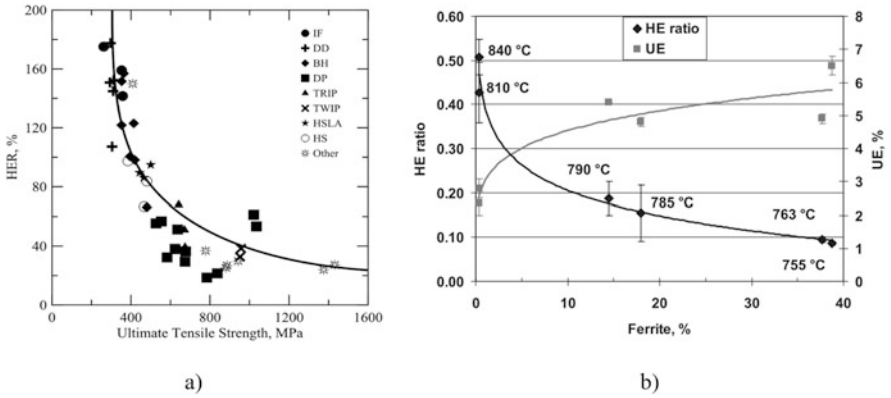

Fig. 4.42 (**a**) Hole expansion ratio (HER) as a function of ultimate tensile strength for a variety of steel grades. Figure from [108] based on data from [107], (**b**) hole expansion ratio (left axis) and uniform elongation (UE-right axis) as a function of ferrite content in DP steels [109]

including DP and TRIP steels, which are examples of so-called first-generation AHSS; TWIP steels are of the second generation; and TBF, Q&P, and medium manganese steels among other concepts are being explored as third-generation AHSS. These various steels require different alloying and heat-treating strategies that were reviewed along with their microstructural characteristics. Substantial development and implementation efforts are underway toward increased usage of AHSS in vehicle architectures.

Acknowledgments The support of the sponsors of the Advanced Steel Processing and Products Research Center, an NSF industry-university cooperative research center at Colorado School of Mines, is gratefully acknowledged. Brandon Blesi is gratefully acknowledged for his work on redrawing Fig. 4.7.

References

1. Setting emission performance standards for new passenger cars as part of the Community's integrated approach to reduce CO_2 emissions from light-duty vehicles, Regulation (EC) No 443/2009 of the European parliament and of the council, April 23, 2009
2. Environmental Protection Agency (EPA), Department of Transportation (DOT), National Highway Traffic Safety Administration (NHTSA), 2017 and Later Model Year Light-Duty Vehicle Greenhouse Gas Emissions and Corporate Average Fuel Economy Standards. USA Fed. Reg. **77**, 62624–63200 (2012)
3. European Environment Agency, Average CO_2 emissions from newly registered motor vehicles, (2018)
4. Regulation (EU) No 510/2011 of the European Parliament and of the Council of 11 May 2011 setting emission performance standards for new light commercial vehicles as part of the Union's integrated approach to reduce CO_2 emissions from light-duty vehicles, Official Journal of the European Union, pp. L 145/1–18, 2011
5. J. Miller, N. Lutsey, *Consumer Benefits of Increased Efficiency in 2025–2030 Lightduty Vehicles in the U.S* (International Council on Clean Transportation, 2017)
6. "Advanced High Strength Steel (AHSS) Application Guidelines", International Iron & Steel Institute, Committee on Automotive Applications, available online at www.worldautosteel.org
7. D.K. Matlock, J.G. Speer, Design Considerations for the Next Generation of Advanced High Strength Sheet Steels, in *Proceedings of the 3rd International Conference on Structural Steels*, ed. by H. C. Lee, (The Korean Institute of Metals and Materials, Seoul, Korea, 2006), pp. 774–781
8. C.D. Horvath, J.R. Fekete, Opportunities and Challenges for Increased Usage of Advanced High Strength Steels in Automotive Applications, in *International Conference on Advanced High Strength Sheet Steels for Automotive Applications Proc*, ed. by J. G. Speer, (AIST, Warrendale, PA, 2004), pp. 3–10
9. C.D. Horvath, C.M. Enloe, J.P. Singh, J.J. Coryell, Persistent Challenges to Advanced High-Strength Steel Implementation, in *Proceedings, International Symposium on New Developments in Advanced High-Strength Sheet Steels*, ed. by E. De Moor, N. Pottore, G. Thomas, M. Merwin, J. G. Speer, (AIST, Warrendale, PA, 2017), pp. 1–10
10. W.S. Miller, L. Zhuang, J. Bottema, A.J. Wittebrood, P. De Smet, A. Haszler, A. Vieregge, Recent development in aluminium alloys for the automotive industry. Mater. Sci. Eng. A **280**, 37–49 (2000)
11. J. Hirsch, Recent development in aluminium for automotive applications. Trans. Nonferrous Met. Soc. China **24**, 1995–2002 (2014)
12. J.C. Benedyk, Aluminum alloys for lightweight automotive structures, in *Materials, Design and Manufacturing for Lightweight Vehicles*, ed. by P. K. Mallick, (Woodhead Publishing Limited, 2010), pp. 79–113
13. B.C. De Cooman, Y. Estrin, S.K. Kim, Twinning-induced plasticity (TWIP) steels. Acta Mater. **142**, 283–362 (2018)
14. R. Rana, S.B. Singh (eds.), Automotive Steels-Design, Metallurgy, Processing and Applications, Woodhead Publishing Series in Metals and Surface Engineering (2017)
15. D.K. Matlock, J.G. Speer, Third Generation of AHSS: Microstructure Design Concepts, in *Microstructure and Texture in Steels*, ed. by A. Haldar, S. Suwas, D. Bhattacharjee, (Springer,

London, 2009), pp. 185–205
16. A. T. Davenport (ed.), *Formable HSLA and Dual-Phase Steels* (TMS-AIME, Warrendale, PA, 1977)
17. R. A. Kot, J. W. Morris (eds.), *Structure and Properties of Dual-Phase Steels* (TMS-AIME, Warrendale, PA, 1979)
18. R. A. Kot, B. L. Bramfitt (eds.), *Fundamentals of Dual-Phase Steels* (TMS-AIME, Warrendale, PA, 1981)
19. A.K. De, J.G. Speer, D.K. Matlock, Color tint-etching for multiphase steels. Adv. Mat. Proc. **161**, 27–30 (2003)
20. R. Kuziak, R. Kawalla, S. Waengler, Advanced high strength steels for automotive industry. Arch. Civ. Mech. Eng. **8**, 103–117 (2008)
21. N. Fonstein, Advanced high strength sheet steels-physical metallurgy, design, processing, and properties. Springer
22. R.G. Davies, Influence of Martensite composition and content on the properties of dual phase steels. Metall. Trans. A. **9**, 671–679 (1978)
23. M.S. Rashid, B.V.N. Rao, Tempering Characteristics of a Vanadium-Containing Dual-Phase Steel, in *Fundamentals of Dual-Phase Steels*, ed. by R. A. Kott, B. Bramfitt, (TMS-AIME, Warrendale, PA, 1981), pp. 249–264
24. D.A. Korzekwa, D.K. Matlock, G. Krauss, Dislocation substructure as a function of strain in a dual-phase steel. Metall. Mater. Trans. A **15**, 1221–1228 (1984)
25. V. Zackay, E. Parker, D. Fahr, R. Busch, The enhancement of ductility in high strength steels. Trans. Am. Soc. Met. **60**, 252–259 (1967)
26. J. Mahieu, B.C. De Cooman, J. Maki, Phase transformation and mechanical properties of si-free CMnAl transformation-induced plasticity-aided steel. Metall. Mater. Trans. A **33**, 2573–2580 (2002)
27. W.S. Owen, The effect of silicon on the kinetics of tempering. Trans. Am. Soc. Met. **46**, 812–829 (1954)
28. L. Samek, E. De Moor, J. Penning, B.C. De Cooman, Influence of alloying elements on the kinetics of strain-induced martensitic nucleation in low-alloy, multiphase high-strength steels. Metall. Mater. Trans. A **37**, 109–124 (2006)
29. G.B. Olson, M. Cohen, Kinetics of strain-induced Martensite nucleation. Metall. Trans. A. **6**, 791–795 (1975)
30. P.J. Jacques, Q. Furnémont, F. Lania, T. Pardoen, F. Delannay, Multiscale mechanics of TRIP-assisted multiphase steels: I. Characterization and mechanical testing. Acta Mater. **55**, 3681–3693 (2007)
31. E. De Moor, L. Samek, J. Penning and B.C. De Cooman, Unpublished research
32. J.R. Platel, M. Cohen, Criterion for the action of applied stress in the Martensite transformation. Acta Metall. **1**, 531–538 (1953)
33. G.N. Haidemenopoulos, M. Grujicic, G.B. Olson, M. Cohen, Transformation microyielding of retained austenite. Acta Metall. **37**, 1677–1682 (1989)
34. A.N. Vasilakos, K. Papamantellos, G.N. Haidemenopoulos, W. Bleck, Experimental determination of the stability of retained austenite in low alloy TRIP steels. Steel Res. Intl. **70**, 466–471 (1999)
35. G.B. Olson, Mechanically-Induced Phase Transformation in Alloys, in *Encyclopedia of Materials: Science and Technology*, ed. by M. B. Bever, (Pergamon Press, Cambridge, MA, 1986), pp. 2929–2932

36. L. Barbé, M. De Meyer, B.C. De Cooman, *Determination of the Msσ Temperature of Dispersed Phase TRIP-Aided Steels, in: International Conference on TRIP-Aided High Strength Ferrous Alloys* (Gent, Belgium, 2002)
37. L. Barbé, M. De Meyer, B.C. De Cooman, Determination of the M_S^σ temperature of dispersed phase TRIP-aided steels, in *Proceedings International Conference on TRIP-Aided High Strength Ferrous Alloys*, ed. by B. C. De Cooman, (GRIPS, 2002), pp. 65–70
38. J. Mahieu, PhD thesis, Ghent University
39. J. Van Slycken, P. Verleysen, J. Degrieck, J. Bouquerel, B.C. De Cooman, Dynamic response of aluminium containing TRIP steel and its constituent phases. Mater. Sci. Eng. A **460–461**, 516–524 (2007)
40. L. Samek, E. De Moor, B.C. De Cooman, J. Van Slycken, P. Verleysen, J. Degrieck, Quasi-adiabatic Effects During the High Strain Rate Deformation of Dispersed-phase Ferrous Alloys with Strain Induced Martensitic Transformation, in *Intl. Conf. on Advanced High Strength Sheet Steels for Automotive Applications Proceedings*, ed. by AIST, (2004), pp. 361–374
41. T.M. Link, G. Chen, Anisotropy Effects in the Axial Crash Behavior of Advanced High-Strength Steels, in *Proceedings International Symposium on New Developments in Advanced High-Strength Sheet Steels*, (AIST, Warrendale, PA, 2013), pp. 63–70
42. K.-I. Sugimoto, T. Iida, J. Sakaguchi, T. Kashima, Retained austenite characteristics and tensile properties in a TRIP type Bainitic sheet steel. ISIJ Int. **40**, 902–908 (2000)
43. J.G. Speer, D.K. Matlock, B.C. De Cooman, J.G. Schroth, Carbon partitioning into austenite after Martensite transformation. Acta Mater. **51**, 2611–2622 (2003)
44. A.M. Streicher, J.G. Speer, D.K. Matlock, B.C. De Cooman, *Proceedings of the International Conference on Advanced High Strength Sheet Steels for Automotive Applications* (AIST, Warrendale, PA, June 6–9, Winter Park, CO, 2004), pp. 51–62
45. D.V. Edmonds, K. He, F.C. Rizzo, B.C. De Cooman, D.K. Matlock, J.G. Speer, Mater. Sci. Eng. **A438-440**, 25–34 (2006)
46. D.K. Matlock, V.E. Bräutigam, J.G. Speer, Application of the quenching and partitioning (Q&P) process to a medium-carbon, high-Si microalloyed Bar steel. Mater. Sci. For. **426–432**, 1089–1094 (2003)
47. E. De Moor, S. Lacroix, A.J. Clarke, J. Penning, J.G. Speer, Effect of retained austenite stabilized via quench and partitioning on the strain hardening of martensitic steels. Metall. Mater. Trans. A **39**, 2586–2595 (2008)
48. E. De Moor, J. Kähkönen, P. Wolfram, J.G. Speer, Current Developments in Quenched and Partitioned Steels, in *Proc. of the 5th Intl. Symposium on Steel Science, 2017, Nov. 13–16*, ed. by The Iron and Steel Institute of Japan, (Kyoto, Japan, 2017), pp. 11–17
49. D.T. Pierce, D.R. Coughlin, D.L. Williamson, K.D. Clarke, A.J. Clarke, J.G. Speer, E. De Moor, Characterization of transition carbides in quench and partitioned steel microstructures by Mössbauer spectroscopy and complementary techniques. Acta Mater. **90**, 417–430 (2015)
50. J.G. Speer, A.M. Streicher, D.K. Matlock, F. Rizzo, G. Krauss, Quenching and Partitioning: A fundamentally new process to create high strength TRIP sheet microstructures, in *Formation and Decomposition*, ed. by Austenite, (TMS/ISS, Warrendale, PA, 2003), pp. 505–522
51. E. De Moor, J.G. Speer, D.K. Matlock, J.H. Kwak, S.B. Lee, Effect of carbon and manganese on the quenching and partitioning response of CMnSi steels. ISIJ Int **51**, 137–144 (2011)
52. R.L. Miller, Ultra-fine grained microstructures and mechanical properties of alloy steels. Metall. Trans. **3**, 905–912 (1972)
53. E. De Moor, D.K. Matlock, J.G. Speer, M.J. Merwin, Austenite stabilization through manganese enrichment. Scri. Mater. **64**, 185–188 (2011)
54. M.J. Merwin, Microstructure and Properties of Cold Rolled and Annealed Low-Carbon Manganese TRIP Steels, in *Proc. of Materials Science and Technology 2007, Sept. 16–20*, (Detroit, MI, 2007), pp. 515–536
55. S. Lee, S.-J. Lee, B.C. De Cooman, Austenite stability of ultrafine-grained transformation-induced plasticity steel with Mn partitioning. Scri Mater. **65**, 225–228 (2011)

56. P.J. Gibbs, E. De Moor, M.J. Merwin, B. Clausen, J.G. Speer, D.K. Matlock, Austenite stability effects on tensile behavior of manganese-enriched-austenite transformation-induced plasticity steel. Metall. Mater. Trans. A **42**, 3691–3702 (2011)
57. W. Gan, S.S. Babu, N. Kapustka, R.H. Wagoner, Microstructural effects on the springback of advanced high-strength steel. Metall. Trans. A **37**, 3221–3231 (2006)
58. A.W. Hudgins, D.K. Matlock, J.G. Speer, C.J. Van Tyne, Predicting instability at die radii in advanced high strength steels. J. Mater. Proc. Tech. **210**, 741–750 (2010)
59. T. Taylor, A. Clough, Critical review of automotive hot-stamped sheet steel from an industrial perspective. Mater. Sci. Tech. **34**, 809–861 (2018)
60. A. Erman Tekkaya, H. Karbasian, W. Homberg, M. Kleiner, Thermo-mechanical coupled simulation of hot stamping components for process design. Prod. Eng. Res. Devel. **1**, 85–89 (2007)
61. M. Suehiro, K. Kusumi, T. Miyakoshi, J. Maki, M. Ohgami, Properties of Aluminium-coated steels for hot-forming. Nippon Steel Tech. Rep. **88**, 16–21 (2003)
62. G. Frommeyer, U. Brüx, P. Neumann, Supra-ductile and high-strength manganese-TRIP/TWIP steels for high energy absorption purposes. ISIJ Intl. **43**, 438–446 (2003)
63. O. Grässel, L. Krüger, G. Frommeyer, L.W. Meyer, High strength Fe-Mn-(Al,Si) TRIP/TWIP steels development – properties - application. Int. J. Plast. **16**, 1391–1409 (2000)
64. U. Brux, G. Frommeyer, O. Grassel, L.W. Meyer, A. Weise, Development and characterization of high strength impact resistant Fe-Mn-(Al-, Si) TRIP/TWIP steels. Steel Res. Intl. **73**, 294–298 (2002)
65. S. Martin, S. Wolf, U. Martin, L. Krüger, D. Rafaja, Deformation mechanisms in austenitic TRIP/TWIP steel as a function of temperature. Metall. Mater. Trans. A **47**, 49–58 (2016)
66. S. Martin, C. Ullrich, D. Rafaja, Deformation of austenitic CrMnNi TRIP/TWIP steels: Nature and role of the $\varepsilon-$martensite. Mat. Today Proc. **2S**, S643–S646 (2015)
67. L. Krüger, L.W. Meyer, U. Brûx, G. Frommeyer, O. Grässel, Stress-deformation behaviour of high manganese (AI, Si) TRIP and TWIP steels. J. Phys. IV France **110**, 189–194 (2003)
68. S.-M. Lee, S.-J. Lee, S. Lee, J.-H. Nam, Y.-K. Lee, Tensile properties and deformation mode of Si-added Fe-18Mn-0.6C steels. Acta Mater. **144**, 738–747 (2018)
69. J.A. Ronevich, J.G. Speer, D.K. Matlock, "Hydrogen embrittlement of commercially produced advanced high strength sheet steels," SAE technical publication #2010-01-0447. SAE Int. J. Mater. Manuf. **3**, 255–267 (2010)
70. S. Kang, Y.-S. Jung, J.-H. Jun, Y.-K. Lee, Effects of recrystallization annealing temperature on carbide precipitation, microstructure, and mechanical properties in Fe–18Mn–0.6C–1.5Al TWIP steel. Mater. Sci. Eng. A **527**, 745–751 (2010)
71. L. Bracke, K. Verbeken, L. Kestens, J. Penning, Recrystallization behaviour of an austenitic high Mn steel. Mater. Sci. For. **558–559**, 137–142 (2007)
72. J.-H. Kang, T. Ingendahl, W. Bleck, A constitutive model for the tensile behaviour of TWIP steels: Composition and temperature dependencies. Mater. Des. **90**, 340–349 (2016)
73. W.S. Choi, B.C. De Cooman, S. Sandlöbes, D. Raabe, Size and orientation effects in partial dislocation-mediated deformation of twinning-induced plasticity steel micro-pillars. Acta Mater. **98**, 391–404 (2015)
74. I.-C. Jung, B.C. De Cooman, Temperature dependence of the flow stress of Fe–18Mn–0.6C–xAl twinning-induced plasticity steel. Acta Mater. **61**, 6724–6735 (2013)
75. B. Mahatoa, S.K. Shee, T. Sahu, S. Ghosh Chowdhury, P. Sahu, D.A. Porter, L.P. Karjalainen, An effective stacking fault energy viewpoint on the formation of extended defects and their contribution to strain hardening in a Fe–Mn–Si–Al twinning-induced plasticity steel. Acta Mater. **86**, 69–79 (2015)
76. H. Idrissi, K. Renard, L. Ryelandt, D. Schryvers, P.J. Jacques, On the mechanism of twin formation in Fe–Mn–C TWIP steels. Acta Mater. **58**, 2464–2476 (2010)
77. S. Mahajan, G.Y. Chin, Formation of deformation twins in f.c.c. crystals. Acta Metall. **21**, 1353–1363 (1973)
78. J.-E. Jin, Y.-K. Lee, Effects of Al on microstructure and tensile properties of C-bearing high Mn TWIP steel. Acta Mater. **60**, 1680–1688 (2012)

79. J.S. Jeong, W. Woo, K.H. Oh, S.K. Kwon, Y.M. Koo, In situ neutron diffraction study of the microstructure and tensile deformation behavior in Al-added high manganese austenitic steels. Acta Mater. **60**, 2290–2299 (2012)
80. J. Kim, S.-J. Lee, B.C. De Cooman, Effect of Al on the stacking fault energy of Fe–18Mn–0.6C twinning-induced plasticity. Scri. Mater. **65**, 363–366 (2011)
81. C. Scott, B. Remy, J.-L. Collet, A. Cael, C. Bao, F. Danoix, B. Malar, C. Curfs, Precipitation strengthening in high manganese austenitic TWIP steels. Int. J. Mater. Res. **102**, 538–549 (2011)
82. L. Rémy, A. Pineau, Twinning and strain-induced f.c.c. → h.c.p. transformation on the mechanical properties of co-Ni-Cr-Mo alloys. Mater. Sci. Eng. **26**, 123–132 (1976)
83. L. Rémy, The interaction between slip and twinning systems and the influence of twinning on the mechanical behavior of fcc metals and alloys. Metall. Trans. A. **12**, 387–408 (1981)
84. S. Allain, J.-P. Chateau, O. Bouaziz, A physical model of the twinning-induced plasticity effect in a high manganese austenitic steel. Mater. Sci. Eng. A **387**, 143–147 (2004)
85. T.-H. Lee, E. Shin, C.-S. Oh, H.-Y. Ha, S.-J. Kim, Correlation between stacking fault energy and deformation microstructure in high-interstitial-alloyed austenitic steels. Acta Mater. **58**, 3173–3186 (2010)
86. O. Bouaziz, S. Allain, C.P. Scott, P. Cugy, D. Barbier, High manganese austenitic twinning induced plasticity steels: A reviewof the microstructure properties relationships. Curr. Opin. Solid State Mater. Sci. **15**, 141–168 (2011)
87. L. Bracke, L. Kestens, J. Penning, Transformation mechanism of α'-martensite in an austenitic Fe–Mn–C–N alloy. Scri. Mater. **57**, 385–388 (2007)
88. T. Michler, C. San Marchi, J. Naumann, S. Weber, M. Martin, Hydrogen environment embrittlement of stable austenitic steels. Intl. J. Hydrogen Energy **37**, 16231–16246 (2012)
89. M. Koyama, E. Akiyama, K. Tsuzaki, Hydrogen embrittlement in a Fe–Mn–C ternary twinning-induced plasticity steel. Corr. Sci. **54**, 1–4 (2012)
90. J.K. Jung, O.Y. Lee, Y.K. Park, D.E. Kim, K.G. Jin, Hydrogen embrittlement behavior of high Mn TRIP/TWIP steels. Korean J. Mater. Res. **18**, 394–399 (2008)
91. S.-k. Kim, G. Kim, K.-g. Chin, Development of High Manganese TWIP Steel with 980MPa Tensile Strength, in *Proceedings of the International Conference on New Developments in Advanced High-Strength Sheet Steels*, (AIST, 2008), pp. 249–258
92. J.A. Ronevich, S.K. Kim, J.G. Speer, D.K. Matlock, Hydrogen effects on cathodically charged twinning-induced plasticity steel. Scri. Mater. **66**, 956–959 (2012)
93. K.H. So, J.S. Kim, Y.S. Chun, K.T. Park, Y.G. Lee, C.S. Lee, Effect of hydrogen on fracture of austenitic Fe–Mn–Al steel. ISIJ Int. **49**, 2009 (1952–1959)
94. J.H. Ryu, S.K. Kim, C.S. Lee, D.-W. Suh, H.K.D.H. Bhadeshia, Effect of Aluminium on hydrogen-induced fracture behaviour in austenitic Fe-Mn-C steel. Proc R Soc A **469**, 20120458 (2013)
95. K.G. Chin, C.Y. Kang, S.Y. Shin, S.K. Hong, S.H. Lee, H.S. Kim, K.H. Kim, N.J. Kim, Effects of Al addition on deformation and fracture mechanisms in two high manganese TWIP steels. Mater. Sci. Eng. A **528**, 2922–2928 (2011)
96. H. Kim, D.-W. Suh, N.J. Kim, Fe–Al–Mn–C lightweight structural alloys: A review on the microstructures and mechanical properties. Sci. Technol. Adv. Mater. **14**, 1–11 (2013)
97. R. Rana, C. Lahaye, R.K. Ray, Overview of lightweight ferrous materials: Strategies and promises. JOM **66**, 1734–1746 (2014)
98. I. Zuazo, B. Hallstedt, B. Lindahl, M. Selleby, M. Soler, A. Etienne, A. Perlade, D. Hasenpouth, V. Massardier-Jourdan, S. Cazottes, X. Kleber, Low-density steels: Complex metallurgy for automotive applications. JOM **66**, 1747–1758 (2014)
99. D. Raabe, H. Springer, I. Gutierrez-Urrutia, F. Roters, M. Bausch, J.-B. Seol, M. Koyama, P.-P. Choi, K. Tsuzaki, Alloy design, combinatorial synthesis, and microstructure–property relations for low-density Fe-Mn-Al-C austenitic steels. JOM **66**, 1845–1856 (2014)
100. R. Rana, C. Liu, R.K. Ray, Low-density Low-carbon Fe–Al Ferritic Steels. Scri. Mater.**68**, 354–359 (2013)

101. O. Ikeda, I. Ohnuma, R. Kainuma, K. Ishida, Phase equilibria and stability of ordered BCC phases in the Fe-rich portion of the Fe–Al system. Intermetallics **9**, 755–761 (2001)
102. Y.-U. Heo, Y.Y. Song, S.-J. Park, H.K.D.H. Bhadeshia, D.-W. Suh, Influence of silicon in low density Fe-C-Mn-Al steel. Metall. Mater. Trans. A **43**, 1731–1735 (2012)
103. M. Chen, D.J. Zhou, "AHSS forming simulation for shear fracture and edge cracking", Great designs in steel. Am. Iron Steel Inst.
104. M. Shi, X. Chen, Prediction of Stretch Flangeability Limits of Advanced High Strength Steels Using the Hole Expansion Test, SAE Technical Paper 2007-01-1693, (2007)
105. R.J. Johnson, *Hole Expansion of Retained Austenite Containing CMnSi Bainitic/Martensitic Steels* (Colorado School of Mines, 2013)
106. C. Butcher, L. ten Kortenaar, M. Worswick, Experimental characterization of the sheared edge formability of boron steel. IDDRG Conf. Proc., 222–227 (2014)
107. S. Sadagopan, D. Urban, *Formability Characterization of a New Generation of High Strength Steels* (US Department of Energy, American Iron and Steel Institute, 2003).
108. O.R. Terrazas, K.O. Findley, C.J. Van Tyne, Influence of martensite morphology on sheared-edge formability of dual-phase steels. ISIJ Int. **57**, 937–944 (2017)
109. I. Pushkareva, C.P. Scott, M. Gouné, N. Valle, A. Redjaïmia, A. Moulin, U. De Lorraine, I. Jean, L. Crns, M. De Nancy, P. De Saurupt, F. Nancy, Distribution of carbon in martensite during quenching and tempering of dual phase steels and consequences for damage properties. ISIJ Int **53**, 1215–1223 (2013)
110. N. Pottore, N. Fonstein, I. Gupta, D. Bhattacharya, A Family of 980MPa Tensile Strength Advanced High Strength Steels with Various Mechanical Property Attributes, in *International Conference on Advanced High Strength Sheet Steels for Automotive Applications Proceedings*, ed. by J. G. Speer, (AIST, Warrendale, PA, 2004), pp. 119–129
111. S.B. Lee, J.G. Speer, D.K. Matlock, K.G. Chin, Analysis of Stretch-Flangeability Using a Ductile Fracture Model, in *3rd International Conference on Advanced Structural Steels*, (2006), pp. 841–849
112. A. Karelova, C. Krempaszky, E. Werner, P. Tsipouridis, T. Hebesberger, A. Pichler, Hole expansion of dual-phase and complex-phase AHS steels - effect of edge conditions. Steel. Res. Int. **80**, 71–77 (2009)